Reproducing pyroclastic density currents deposits of the AD 79 eruption of the Somma-Vesuvius volcano using the box-model approach

Alessandro Tadini[1,2,3], Andrea Bevilacqua[2], Augusto Neri[2], Raffaello Cioni[3], Giovanni Biagioli[4], Mattia de'Michieli Vitturi[2], Tomaso Esposti Ongaro[2]

[1]Laboratoire Magmas et Volcans, Université Clermont Auvergne, CNRS, IRD, OPGC, 6 Avenue Blaise Pascal – 63178 Aubière, France.
[2]Istituto Nazionale di Geofisica e Vulcanologia, Sezione di Pisa, Via Cesare Battisti, 53 – 56125 Pisa, Italy.
[3]Dipartimento di Scienze della Terra, Università di Firenze, Via G. La Pira, 4 – 50121 Firenze, Italy.
[4]Dipartimento di Matematica e Geoscienze, Università degli Studi di Trieste, Via Weiss 2 - 34128 Trieste, Italy.

Correspondence to: Alessandro Tadini (Alessandro.TADINI@uca.fr)

Abstract. In this study we use PyBox, a new numerical implementation of the box-model approach, to reproduce pyroclastic density current (PDC) deposits from the Somma-Vesuvius volcano (Italy). Our simplified model assumes inertial flow front dynamics and mass deposition equations, and axisymmetric conditions inside circular sectors. Tephra volume and density, and Total Grain Size Distribution of EU3pf and EU4b/c, two well-studied PDC units from different phases of the AD 79 Pompeii eruption of Somma-Vesuvius (Italy) are used as input parameters. Such units correspond to the deposits from variably dilute, turbulent PDCs. We perform a quantitative comparison and uncertainty quantification of numerical model outputs with respect to the observed data of unit thickness, inundation areas, and grain size distribution as a function of the radial distance to the source. The simulations that we performed with PyBox were done considering: i) polydisperse conditions, given by the total grain size distribution of the deposit or monodisperse conditions, given by the mean Sauter diameter of the deposit; ii) round-angle axisymmetrical collapses or divided in two circular sectors. We obtain a range of plausible initial volume concentrations of solid particles from 2.5% to 6%, depending on the unit and the circular sector. Optimal modelling results of flow extent and deposit thickness are reached on the EU4b/c unit in a polydisperse and sectorialized situation, indicating that using total grain size distribution and particle densities as close as possible to the real conditions significantly improve the performance of the PyBox code. The study findings suggest that the box model simplified approaches adopted have promising applications in constraining the plausible range of the input parameters of more computationally expensive models.

1 Introduction

The increased availability of numerical models capable of reproducing, with various degrees of simplification, the dynamics of pyroclastic flows, provided geoscientists and civil authorities with new valuable tools for better understanding natural

phenomena and for more accurate hazard assessments. Several modeling approaches have been developed over the past years for Pyroclastic Density Currents (PDCs), from simplified 1D kinetic models (Malin and Sheridan, 1982; Sheridan and Malin, 1983; Dade and Huppert, 1995a, 1996; Bursik and Woods, 1996; Doyle et al., 2010; Esposti Ongaro et al., 2016; Fauria et al., 2016) up to more complex, 2D depth-averaged models (Patra et al., 2005, 2020; Charbonnier and Gertisser, 2009; Kelfoun et al., 2009, 2017; Tierz et al., 2018; de'Michieli Vitturi et al., 2019) and computationally expensive but physically realistic 3D models (Neri et al., 2003; Esposti Ongaro et al., 2007, 2012, 2019).

Although the 1D kinetic approaches cannot capture the multidimensional features of dynamics, they represent an important tool for several purposes. Firstly, it is practical to rely on simplified and fast numerical codes, which can be run 10^4-10^6 times without an excessive computational expense, in order to produce statistically robust probabilistic hazard maps (Neri et al., 2015; Bevilacqua et al., 2017; Aravena et al., 2020). Furthermore, since 2D or 3D multiphase models require high computational times, often on the order of days or weeks for a single simulation, it is convenient to use simplified approaches, such as the box-model, in order to constrain the input space (Ogburn and Calder, 2017; Bevilacqua et al., 2019a). Finally, extensively testing the numerical models in a statistical framework, and evaluating the difference between model outputs and actual observations, also allows estimating the effect of the various modeling assumptions under uncertain input conditions (e.g., Patra et al., 2018, 2020; Bevilacqua et al., 2019b). Model uncertainty is probably the most difficult class of epistemic uncertainty to evaluate robustly, but it is indeed a potentially large component of the total uncertainty affecting PDC inundation forecasts.

In this paper, we test the suitability of box-model approach (described in section 2.1 and in Appendix A), as implemented numerically in the PyBox code (Biagioli et al., 2019), by quantifying its performance when reproducing some key features of the remarkably well-known PDC deposits from one of the best studied and documented volcanic events, the AD 79 eruption of the Somma-Vesuvius (SV) volcano (detailed in section 2.2). It is indeed accepted that the box model is able to describe the main features of large-volume (VEI 6 to 8; Newhall and Self, 1982), low aspect ratio ignimbrites, whose dynamics is dominantly inertial (Dade and Huppert, 1996). However, the model has never been tested again PDC generated by VEI 5 Plinian eruptions. The procedure involves the calculation of the difference between model output and field data in terms of i) thickness profile, ii) areal invasion overlapping and iii) grain sizes (GS) volume fractions at various distances from the source. Similar approaches have been adopted in literature (Dade and Huppert, 1996; Kelfoun, 2011; Charbonnier et al., 2015). Tierz et al. (2016a,b) and Sandri et al. (2018) proposed a quantification of the uncertainty derived from the energy cone approach that relies on the comparison between invaded area and maximum runout of model output and field data. Our approach aims at the more detailed comparison of physical parameters (especially thickness and grain sizes, section 5), which allows a further investigation of the strengths and limitations of the PyBox model when used to simulate different PDC types (section 6).

2 Numerical model and data sources

2.1 The box-model approach and the PyBox code

65   ~~The~~ PyBox ~~code,~~ is a numerical implementation of the box-model integral formulation for axisymmetric, gravity-driven particle currents based on the pioneering work of Huppert and Simpson (1980). The theory is detailed in Bonnecaze et al. (1995) and Hallworth et al. (1998). The volume extent of gravity currents is approximated by an ideal geometric element, called "box", which preserves its volume and geometric shape class, and only changes its height/base ratio through time (~~see~~ Figure 1). The box does not rotate or shear, but only stretches out as the flow progresses. In this study the geometric shape of

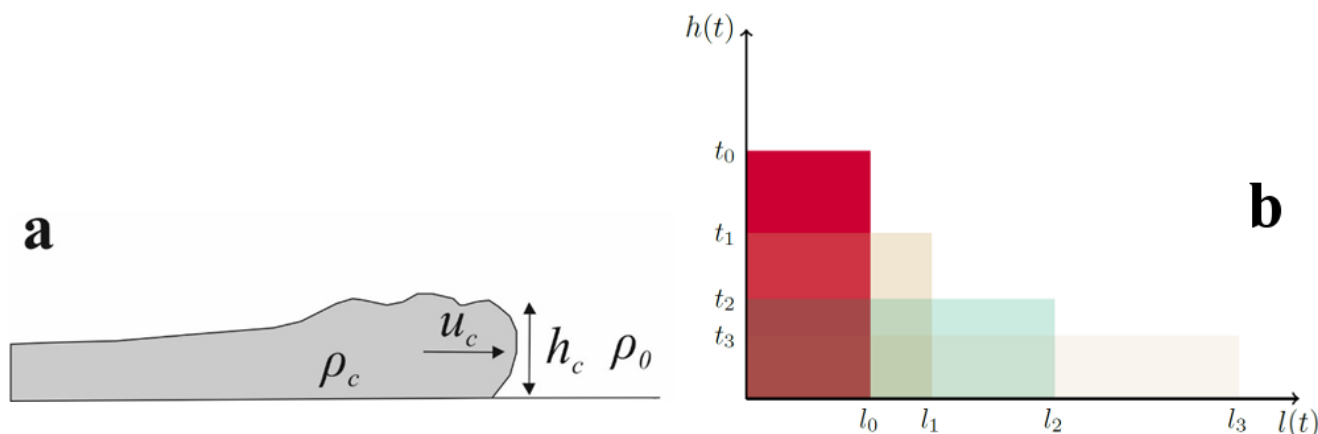70   the box is assumed to be a cylinder, ~~or cylindrical sector,~~ i.e. we assume axisymmetric conditions.

Figure 1. a) Schematic diagram of an inertial gravity current with a depth h_c, flow front velocity u_c and density ρ_c in an ambient fluid of density ρ_0 (modified from Roche et al., 2013); b) Evolution of channelized currents through a series of equal-area rectangles, according to the model (hence the name "box model").

75

The model describes the propagation of a turbulent particle-laden gravity current, i.e. a homogeneous fluid with suspended particles. Inertial effects are assumed to ~~have a leading role~~ with respect to viscous forces and particle-particle interactions. ~~Thus, the p~~article sedimentation is modelled and modifies the current inertia during propagation. In this study we assume the classical dam break configuration, in which a column of fluid instantaneously collapses and propagates, under gravity, in a

80   surrounding atmosphere with uniform density ρ_{atm}. Other authors (Bonnecaze et al., 1995; Dade and Huppert, 1995a, b, 1996) have instead considered gravity currents produced by the constant flux release of dense suspension from a source. Our approach ~~differs from considering~~ constant stress acting on the basal area (Dade and Huppert, 1998). Constant stress dynamics have been ~~further~~ explored in literature, and they can lead to different equations if the basal area grows linearly or with the square of the radius (Kelfoun et al., 2009; Kelfoun, 2011; Ogburn and Calder, 2017; Aspinall et al., 2019).

Solid Earth
Discussions

Open Access

EGU

85 Our model consists of a set of ordinary differential equations, that provide the time evolution of flow front distance from the source, l(t), together with the current height h(t) and the solid particle volume fraction $(\varepsilon_i)_{i=1,...,N}$, N being the number of particle classes considered. The volume fractions refer to a constant volume of the mixture flow, not reduced by the deposition.

PDCs are driven by their density excess with respect to the surrounding air; the density of the current ρ_c is defined as the sum

90 of the density of an interstitial gas, ρ_g, and the bulk densities of the pyroclasts carried by the flow, $(\rho^s_i)_{i=1,...,N}$. In this study we assume $\rho_{atm} \neq \rho_g$, i.e. the interstitial gas is hotter than surrounding atmosphere, differently from Neri et al. (2015) and Benjilcqua et al. (2017). The code allows $\rho_{atm} > \rho_g$, but thermal properties remain constant for the duration of the flow, and in this study we assumed $\rho_{atm} = \rho_g$. The thermodynamics of cooling effects are explored in Bursik and Woods (1996). A proper way to express the density contrast between the current and the ambient fluid is given by the reduced gravity g', that

95 can be rewritten in terms of the densities and the volume fractions described above (see Biagioli et al., 2019). That said, we make some additional simplifying hypotheses, First of all, we assume that the mixture flow regime is incompressible and inviscid, since we assume that the dynamics of the current is dominated by the balance between inertial and buoyancy forces. The assumption of incompressibility implies that the initial volume V_0 remains constant. Moreover, we assume that, within the current, the vertical mixing, due to turbulence, produces a vertically uniform distribution of particles. The particles are

100 assumed to sediment out of the current at a rate proportional to their constant terminal (or settling) velocity $(w^s_i)_{i=1,...,N}$. Once deposited, they cannot be re-entrained by the flow; the converse is explored in (see Fauria et al., 2016). Finally, surface effects of the ambient fluid are neglected.

Under these hypotheses, the box model for particle-laden gravity currents states that the velocity of the current front (u) is related to the average depth of the current (h) by the von Kármán equation for density currents $u = Fr(g'h)^{\frac{1}{2}}$, where Fr is

105 the Froude number, a dimensionless number expressing the ratio between inertial and buoyancy forces (Benjamin, 1968; Huppert and Simpson, 1980) and g' is the reduced gravity. In addition, we assume that particles can settle to the ground and this process changes the solid particle fractions $(\varepsilon_i)_{i=1,...,N}$.

The box model for axisymmetric currents thus reads:

110 $$\frac{dl}{dt} = Fr(g'h)^{\frac{1}{2}} \qquad \text{Eq. (1)}$$

$$l^2 h = l_0^2 h_0 \qquad \text{Eq. (2)}$$

$$\frac{d(\varepsilon_i)}{dt} = \frac{w^s_i \varepsilon_i}{h} \quad \forall\, i = 1,....,N \qquad \text{Eq. (3)}$$

115

By solving these equations, we computed the amount of mass loss by sedimentation, per unit area, per time step, for each particle class. So, the thickness profile of the ith particle class is the ratio of the ith deposited mass to the ith solid density multiplied by the packing fraction α measured in the deposit. More details on the numerical solver are provided in Appendix A.

120   In the calculation of the region invaded by a PDC, first we calculate the maximum flow runout over flat, i.e. the distance at which $\rho_c = \rho_{atm}$. The flow stops propagating when the solid fraction becomes lower than a critical value, and the remaining mixture of gas and particles lifts off, possibly generating a phoenix cloud if hot gas is assumed. In the case of monodisperse systems there are analytical solutions for the maximum flow runout (Bonnecaze et al., 1995; Esposti Ongaro et al., 2016; Bevilacqua, 2019). Then, once set a vent location, we assess the capability of topographic reliefs to block the current. In

125   particular, the invasion areas are obtained by using the so-called energy-conoid model, based on the assumption of non-linear, monotonic decay of flow kinetic energy with distance (Neri et al., 2015; Bevilacqua, 2016; Esposti Ongaro et al., 2016; Bevilacqua et al., 2017; Aspinall et al., 2019; Aravena et al., 2020). In more detail, first we determine the maximum height h_{max} of an obstacle the flow can overcome. Then we compare the kinetic energy of the current front and the potential energy associated to the obstacle top. In this approach we are neglecting returning waves. When investigating the current

130   flow on complex topographies, we finally consider that the flow may start from positive elevation or encounter upward slopes after downward slopes. In this case, we compare h_{max} at a given distance from the vent and the difference in level experienced by the current between the previous and the present sampled positions.

In the PyBox code, the main input parameters are summarized by: a) the total collapsing volume (expressed in terms of the dimension of the initial cylinder/rectangle with height=h_0 and radius/base=l_0); b) the initial concentration of solid particles,

135   subdivided (for polydisperse simulations) into single particle volumetric fractions (ε_0), with respect to the gas; c) the density of single particles ρ_s; d) ambient air density (ρ_{atm}=1.12 kg/m^3) and gravity current temperature; e) Froude number of the flow, experimentally measured by Esposti Ongaro et al. (2016) as Fr=1.18; g) gravity acceleration (g=9.81 m/s^2). With respect to points b) and c), more details are provided in section 3.2.

2.2 The EU3pf and EU4b/c units from the AD 79 eruption of SV

140   The AD 79 eruption of SV volcano (Fig. 2a) was characterized by a complex sequence of fallout and PDC phases, resulting in the deposition of a complex sequence of Eruptive Units (EU; Cioni et al., 1992). The EU3pf and EU4b/c units (Fig. 2b) represent the two main PDC deposits, which have been traced over a large area around the volcano and characterized for their most relevant physical parameters (Gurioli et al., 2010; Cioni et al., 2020).
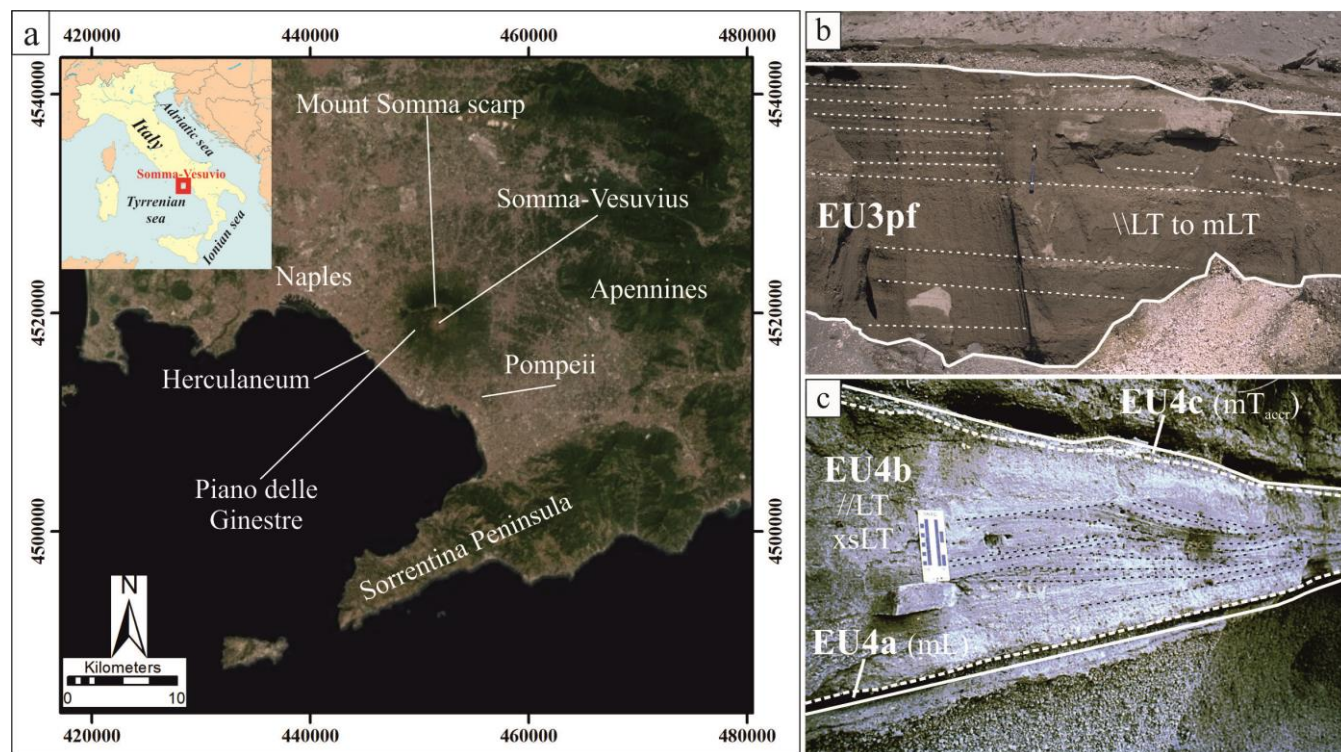
Figure 2. a) Location of the Somma-Vesuvius volcano. Coordinates are expressed in the UTM WGS84-33N system; b) the EU3pf unit (Cioni et al., 2020); c) the EU4 unit (Cioni et al., 2020). Lithofacies terminology is derived from Branney and Kokelaar (2002): //LT "plain parallel lapilli-tuff", mLT "massive lapilli-tuff", xsLT "cross-stratified lapilli-tuff", mL "massive lapillistone", mT$_{accr}$ "massive tuff with accretionary lapilli".

The ~~PDC deposits of the~~ EU3pf unit record the phase of total column collapse closing the Plinian phase of the eruption. These are ca. 1 m thick on average, radially dispersed (up to 10 km from vent area) and moderately controlled by local topography~~, so resulting in a complex~~ vertical and lateral facies ~~variability~~ (Gurioli, 1999; Gurioli et al., 1999) ~~possibly~~ related to local variation in turbulence, concentration and stratification of the current. Median clast size ~~tends to diminish~~ gradually from proximal to distal locations, and the coarsest deposits (generally present as breccia lenses in the EU3pf sequence) are located within paleodepressions. Gurioli et al. (1999) ~~pointed out that: i) in the southern part of the~~ SV ~~area~~ the relatively smooth paleo-topography ~~controlled~~ only locally the overall deposition of this PDC; ~~ii) in~~ the eastern sector of SV, the interaction of the current with the ridge representing the remnants of the old Mount Somma caldera (Fig. 2a) possibly triggered a general increase of the current turbulence and velocity and a more efficient air ingestion which resulted in the local deposition of a thinly stratified sequence; ~~iii) in the western sector of SV,~~ the presence of a breach in the caldera wall and of an important break in slope in the area of Piano delle Ginestre (Fig. 2a), possibly increased deposition from the PDC, producing a large, several meters thick depositional fan toward the sea-facing sectors (like in Herculaneum — Fig. 2a); ~~iv) in~~

6

the northern sector of SV, the deeply eroded paleotopography (with many valleys cut on steep slopes) favoured the development within the whole current of a fast-moving, dense basal underflow able to segregate the coarse, lithic material and to deposit thick lobes in the main valleys, and of a slower and more dilute portion travelling and depositing thin,

165   stratified beds also on morphological highs.

The AD 79 EU4 marks the reappraisal of the eruption after the end of the Plinian phase and was related by Cioni et al. (1999) to the onset of the caldera collapse. This complex unit has been subdivided into three distinct layers (Cioni et al., 1992): a thin basal fallout layer ("EU4a"), a PDC deposit derived from the collapse of the short-lived column that emplaced the EU4a layer ("EU4b"), and the products of the co-ignimbritic plume mainly derived by ash elutriation from the current

170   depositing EU4b ("EU4c"). Gurioli (1999) illustrates how the EU4 unit is furthermore complicated, since it actually presents a second fallout bed ("EU4a2") interlayered within the level "EU4b". This fallout bed can be clearly recognized only in distal sections of the southern sector, while in the north and in the west it is represented by a discontinuous level of ballistic ejecta. Level "a2" divides level "b" in two parts, which are approximately 2/3 (the lower one) and 1/3 (the upper one) of the total thickness of level "b" (Gurioli, 1999). Runout of the EU4b PDC is one of the largest runouts observed for the SV

175   PDCs; it was maximum toward south (up to about 20 km from vent area; Gurioli et al., 2010). This unit has been extensively studied by Gurioli (1999) who highlighted that the high shear rate exerted by the EU4b is clearly evidenced by the formation of "traction carpets" and local erosion of the pumice-bearing layer of the underlying EU4a. The EU4b deposit can be interpreted as derived from a short-lived sustained, unsteady, density stratified current. From a sedimentological point of view, EU4b shows clear vertical grain size and textural variations, from cross bedded, fine lapilli to coarse ash laminae at

180   the base up to a massive, fine ash-bearing, poorly sorted, matrix-supported bed at top (Gurioli, 1999). During deposition of EU4b, ash elutriated from the current formed a convective plume dispersed from the prevailing winds in a south-eastern direction, which deposited EU4c mainly by fallout. The clear field association of these two deposits (indicated as EU4b/c) gives here the uncommon possibility to evaluate with a larger accuracy two of the most important PDC source parameters: erupted volume and TGSD.

185   **3 Methods**

3.1 Model input parameters and field data for comparison

The main properties of the EU3pf and EU4b/c units, i.e. thicknesses/total volume, maximum runout and total grain size distribution – TGSD, have been calculated in Cioni et al. (2020) and partially processed to fit with PyBox input requirements (see sections 3.1.1 and 3.1.3). Densities of single grain sizes (Barberi et al., 1989; section 3.1.2) and emplacement

190   temperatures of PDCs (T=600 K for both EU3pf and EU4; Cioni et al., 2004) are derived from the literature.

In summary, the total volume, the TGSD, the densities and the temperature obtained from the field data are used as the main inputs of PyBox. Thus, the model produces several outputs: (i) mean unit thickness as a function of the radial distance from the source, (ii) inundated area, (iii) grain size distribution as a function of radial distance from the source. All these outputs

are finally compared to the corresponding field data. The initial volumetric fraction ε_0 of the solid particles over the gas is
195   the main tuning parameter that is explored to fit the outputs with the field data. This procedure is repeated under
monodisperse and polydisperse conditions, and by performing round-angle axisymmetrical collapses or sectorialized
collapses, i.e. divided in two circular sectors with different input parameters.

3.1.1 Thickness, maximum runout and volumes

Cioni et al. (2020) recently revised and elaborated a large amount of field data from EU3pf and EU4b/c (106 and 102
200   stratigraphic sections, respectively), tracing detailed isopach maps and defining the maximum runout distance (the ideal 0 m
isopach) and the related uncertainty. Given the objective difficulty to trace the exact position of a 0 m isopach for the deposit
of a past eruption, Cioni et al. (2020) proposed to define three different outlines of PDC maximum runouts, namely "5th
percentile", "50th percentile" and "95th percentile" (called Maximum Runout Lines, MRLs), basing on the uncertainty
associated to each segment of the proposed 0 m isopach. The MRLs of EU3pf and EU4b are shown in Figure 3c and 3d
205   respectively.

Cioni et al. (2020) also calculated the volumes of both EU3pf and EU4b/c, using these maps to derive a digital elevation
model of the deposits with the triangular irregular network (TIN) method (Lee and Schachter, 1980). In this study, we
considered volume estimations (Table 1) related to the MRL_{50}, i.e. the 50th percentile of the maximum runout distance.

Given the asymmetric shape of unit EU4b/c and, partially, of unit EU3pf, we have calculated also the volumes dividing each
210   unit in two circular sectors: N and S for EU3pf, NW and SE for EU4b/c. These subdivisions have been also used to calculate
the related TGSDs (see unit 3.1.3) and to perform sectorialized simulations (see section 4). Figure 3c,d displays the different
sectors for both EU3pf and EU4b/c for which different volumes have been calculated.

Unit	EU3pf			EU4b/c		
Sector	Total	N	S	Total	NW	SE
Volume (km^3)	0.188	0.096	0.092	0.331	0.180	0.151

Table 1. Volume of the EU3pf and EU4b/c units.
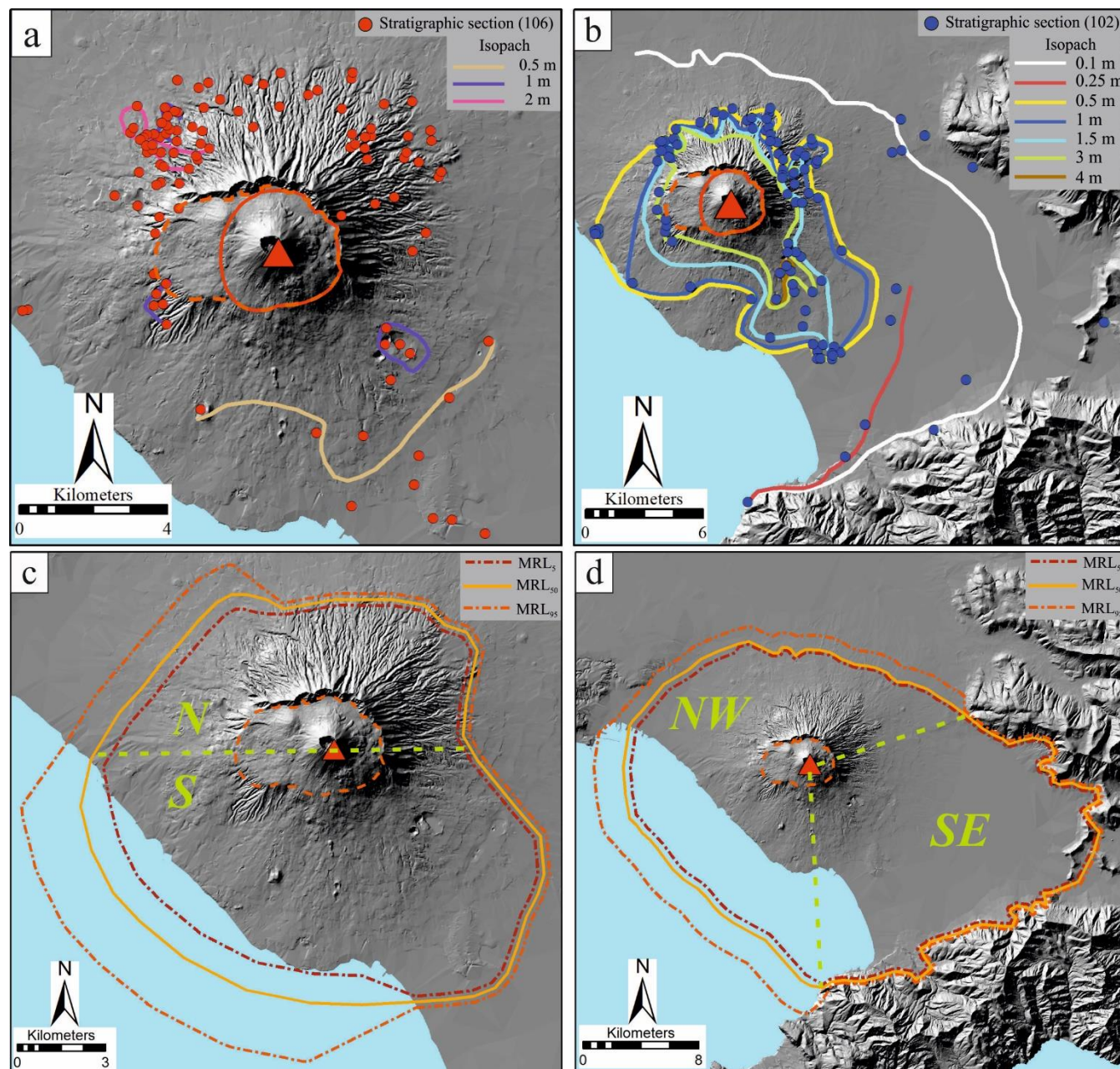
215

8

Figure 3. Thicknesses and isopach lines for the a) EU3pf and b) EU4b/c units; MRLs of the c) EU3pf and d) EU4b/c units. Inferred position of AD 79 vent (red triangle) and SV caldera outline (dark orange dashed line) after Tadini et al. (2017). Light green dashed lines delimit the sectors (N-S for EU3pf and NW-SE for EU4) of the different column collapses. Background DEM from Tarquini et al. (2007).

3.1.2 Density data

In order to provide density values for each GS, we used the mass fractions of the different components (juveniles, lithics and crystals – see Table S1 from the Supporting Information) calculated by Gurioli (1999). Such values were associated to the

225   averaged density measurements for these three components presented in Barberi et al. (1989), through which we extrapolated the weighted mean (with respect to mass fraction) mean density of each grain size class for both EU3pf and EU4b/c units (Table 2).

EU3pf	Φ									
	-4	-3	-2	-1	0	1	2	3	4	5
Weighted mean density (kg/m^3)	1681	1408	1565	1650	1874	2160	2541	2550	2550	2600
EU4b/c	Φ									
	-4	-3	-2	-1	0	1	2	3	4	5
Weighted mean density (kg/m^3)	1855	1532	1804	1851	1839	2103	2519	2495	2590	2600

Table 2. Calculated mean densities for each grain size for both the EU3pf and EU4b/c units.

230   **3.1.3 Grain size data: total grain size distribution (TGSD) and mean Sauter diameter (MSD)**

The TGSD estimations are necessary to do simulations under polydisperse conditions. The present version of PyBox takes as input the volumetric TGSD (i.e. in terms of volumetric percentages), while TGSD data from Cioni et al. (2020) are in weight percentages. These latter values have been therefore converted into volumetric percentages by considering the above-mentioned densities (section 3.1.3). Figure 4 displays the volumetric TGSDs employed for EU3pf (Total, N and S) and the
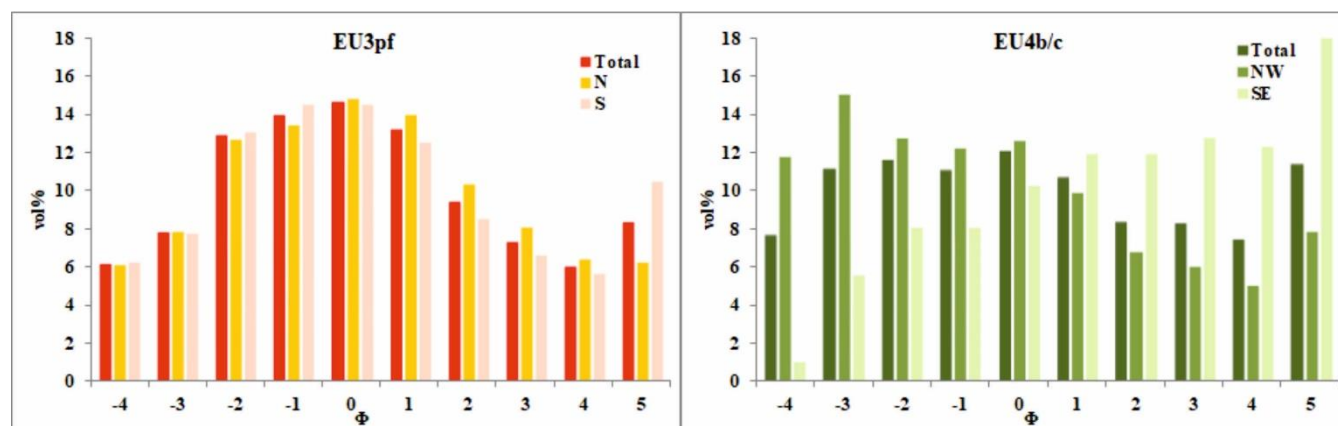
235   EU4b/c (Total, NW and SE).

Figure 4. Volumetric total grain size distributions for the EU3pf and EU4b/c units.

In the simulations under monodisperse conditions, we used the value of mean Sauter diameter (MSD) of the volumetric

240 TGSD (e.g., Neri et al., 2015). According to Fan and Zhu (1998), the Sauter diameter of each particle class size is also called d_{32} (see also Breard et al., 2018), and it is the diameter of a sphere having the same ratio of external surface to volume as the particle, which is given by:

$$d_{32} = \frac{6V}{S} = \frac{d_v^3}{d_s^2} \qquad \text{Eq. (4)}$$

245

where V is the particle volume, S is the particle surface, d_v is the diameter of a sphere having the same volume as the particle and d_s is the diameter of a sphere having the same external surface as the particle. In order to obtain a value for the MSD instead, given a deposit sample divided in N grain size classes, we have initially calculated the number of particles of each grain size i=1,…,N, that is:

250

$$n_i = \frac{V_i}{\frac{4}{3}\pi r_i^3} \qquad \text{Eq. (5)}$$

where V_i is the cumulative volume of the i-th grain size class, and r_i is the radius of the i-th grain size. The mean MSD is finally derived as:

255

$$MSD\ (\Phi) = -log_2 \left(\frac{\sum_{i=1}^N n_i d_i^3}{\sum_{j=1}^N n_j d_j^2} \right) \qquad \text{Eq. (6)}$$

where d_i and d_j are the diameters of, respectively, the i-th and j-th grain sizes.

Table 3 summarizes the calculated MSDs for the studied units (in Φ), along with the corresponding density values (obtained

260 interpolating those in Table 2).

Unit	Sector	MSD (ϕ)	Density (kg/m³)
EU3pf	All	2.34	2327
	N	2.19	2305
	S	2.48	2347
EU4b/c	All	2.63	2374
	NW	2.15	2317
	SE	3.25	2448

Table 3. MSD values and related densities for the different units studied.

3.2 Comparison between field data and simulation outputs

265   Since the PyBox code assumes axisymmetric conditions, the thickness outputs are equal along all the radial directions of the

collapse, and only vary as a function of the distance to the source. These output data were compared with the mean radial

profiles of unit thickness (for both EU3pf and EU4b/c) as derived from the digital models of deposit in Cioni et al. (2020).

For building the radial profiles, the average thickness was estimated over concentric circles drawn with a 100-m step of

distance. The radial thickness profiles were drawn starting from a distance of 3 km from the vent, as no thickness data are

270   available for sites closer than 3 km. ~~Due to the lack of reliable data, we have moreover~~ excluded from our analyses the

portions of the circles located in marine areas. In order to describe the variation range of the thicknesses of the deposits, we

are providing minimum and maximum thicknesses along each circle in Appendix B (Fig. A1).

Concerning the inundation area, the methodology adopted is similar to the one used by Tierz et al. (2016b) and relies on the

275   approach described by Fawcett (2006) and implemented by Cepeda et al. (2010) for landslide deposit back-analysis. This

method is based on the quantification of the areal overlapping between the measured deposit (true classes) and the modelled

deposit (hypothesized classes) (Figure 5). In particular, we quantify: a) the areal percentage of model intersecting the actual

deposit (true positive –TP); b) the areal percentage of model overestimating the actual deposit (false positive – FP); c) the

percentage of model underestimating the actual deposit (true negative – TN). More precisely:

280    $$TP = \left(\frac{Area\,Sim \cap Area\,Dep}{Area\,Sim \cup Area\,Dep}\right) \cdot 100 \qquad FP = \left(\frac{Area\,Sim \setminus Area\,Dep}{Area\,Sim \cup Area\,Dep}\right) \cdot 100 \qquad TN = \left(\frac{Area\,Dep \setminus Area\,Sim}{Area\,Sim \cup Area\,Dep}\right) \cdot 100$$

~~The False Negative case (no deposit nor simulation) has not been obviously calculated.~~ In statistical literature, the True

Positive value is also called Jaccard Index of similarity (Tierz et al., 2016b; Patra et al., 2020). While the TP/TN/FP

approach, and in general the Jaccard Index, focus on the areal overlapping, other metrics can specifically focus on the

distance between the boundaries of the inundated areas, i.e. the Hausdorff distance, detecting and comparing channelized

285   features in the deposit (Aravena et al., 2020). However, PyBox is not specifically aimed at the replication of such features,
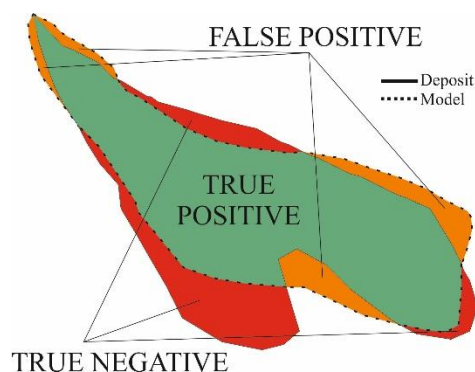
and we focus on the areal overlapping properties.

Figure 5. Sketch representing the three areas used for the validation procedure (the model output outline is drawn in dashed

black line).

290

Finally, the comparison of volume fractions of different GSs has been performed using the mean value of, respectively, ash (< 2 mm of diameter) or lapilli (> 2 mm of diameter) for all the stratigraphic sections in Cioni et al. (2020) placed at similar distances from the vent area. Such values were compared with the corresponding volume fractions of the model at the same distances. More in detail, we considered: i) for the EU3pf unit 18 samples (in sectors N and S) placed at distances from the
295 vent area of 4 km (5 N and 2 S), 6 km (2 S), 7 km (7 S) and 9 km (2 S); ii) for the EU4 unit 19 samples (in sectors NW and SE) placed at distances from the vent area of 4 km (5 NW), 6 km (4 SE), 9 km (5 SE), 14 km (4 SE) and 20 km (1 SE).
The scarcity of stratigraphic sections in the N sector (for the EU3pf unit) and the NW sector (for the EU4b/c unit) negatively affects the availability of comparisons with respect to volume fractions, which are forcedly limited to sections at 4 km of distance from the hypothetical vent area, most of which have been collected at the bottom of paleovalleys. Moreover, for the
300 EU3pf unit, even in the S sector the available samples are mostly concentrated in the area of Herculaneum (5 samples).

4. Results

The results of 6 simulations (4 for the EU3pf unit and 2 for the EU4b/c unit) are discussed here (see Table 4 for the main input parameters). These simulations are the result of an extensive investigation in which a wide range of different values of ε_0 have been tested, following a *trial-and-error* procedure aimed at reproducing more closely the thickness profile of the
305 deposit. In particular, we performed several simulations varying ε_0 between 0.5% and 6% (for EU3pf) and between 0.1% and 5% (for EU4b/c). The values in Table 4 represent the optimal combinations.

| Unit | Simulation Code | Parameters | | | |
		Code type	Collapse type	ε_0	Grain Size(s)
EU3pf	EU3pf_poly_AX	Polydisperse	Axisymmetrical	5%	TGSD
	EU3pf_mono_AX	Monodisperse	Axisymmetrical	5%	MSD
	EU3pf_poly_AS	Polydisperse	AX - Sectorialized	N-6% S-3%	TGSD-N TGSD-S
	EU3pf_mono_AS	Monodisperse	AX - Sectorialized	N-6% S-3%	MSD-N MSD-S
EU4b/c	EU4_poly_AS	Polydisperse	AX - Sectorialized	NW-2.5% SE-2.5%	TGSD-NW TGSD-SE
	EU4_mono_AS	Monodisperse	AX - Sectorialized	NW-2.5% SE-2.5%	MSD-NW MSD-SE

Table 4. PyBox simulations for the EU3pf and EU4b/c units. Symbols key: AX "axisymmetrical"; AS "axisymmetrical-sectorialized"; ε_0 "volumetric fraction of solid particles".

310

We adopted a simplified version of the paleotopography prior to the AD 79 eruption starting from the 10-m resolution Digital Elevation Model of Tarquini et al. (2007) and from the reconstruction given in Cioni et al. (1999) and Santacroce et al. (2003) (Fig. 8). ~~Particularly, the present~~ Gran Cono edifice and part of the caldera morphology have been replaced with a flat area, and a simplified reconstruction of the southern part of the Mount Somma scarp has been inserted. However,

315   simulations performed using the unmodified DEM did not produce major differences.

In the EU3pf case study, we performed both axisymmetrical simulations over a round-angle (given the quasi-circular shape of the deposit) and also axisymmetrical-sectorialized simulations to investigate possible sheltering effects of the Mount Somma scarp (Fig. 2a). ~~In particular,~~ two distinct column collapses, one to the N and the other to the S, each of which has a collapsed volume corresponding to the actual deposit volume in that sector. In the EU4b/c case study, we performed only

320   axisymmetrical-sectorialized simulations, to reproduce more closely the dynamics of the related collapse, as indicated by the different dispersal in the NW and SE sectors of the PDC deposit. In particular, two distinct collapses for the same simulation, one to the NW and the other to the SE)

In summary we provide: a) the thickness comparison between deposit and modelled results (Figure 6) and between simulations done with different initial volumetric fraction of solid particles (ϵ_0 – Figure 7); b) the inundation areas, including

325   the quantitative matching of simulations and actual deposit (Figure 8 and Table 5); c) the grain size distribution comparison, between deposit and modelled values, i.e. the volume fractions of ash vs lapilli (Figure 9) and of all the grain size classes (Figure 10).
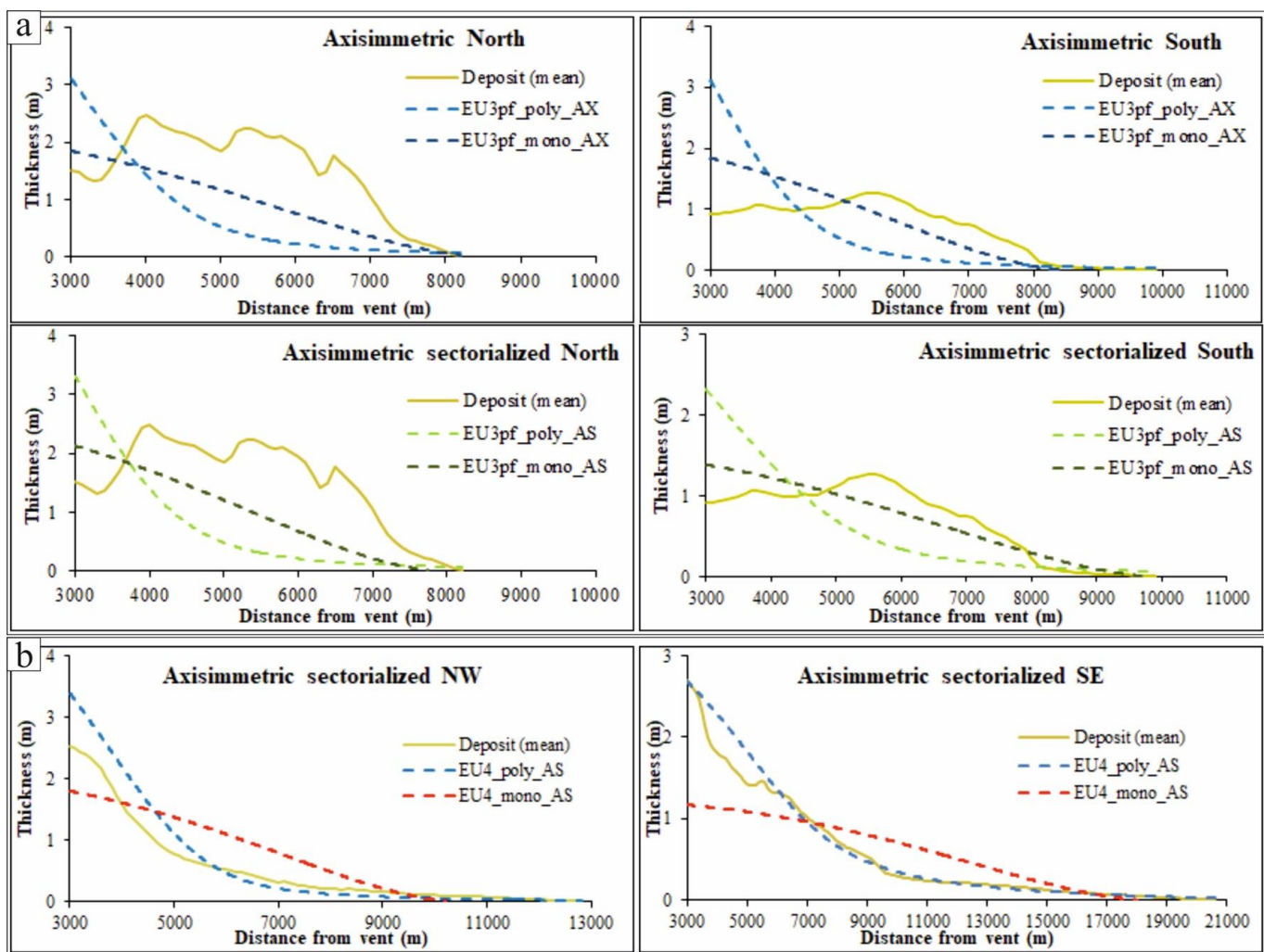
Figure 6. Mean thickness comparison between the simulations (dashed lines) and the actual deposit (solid line) of a) EU3pf and b) EU4b/c units.
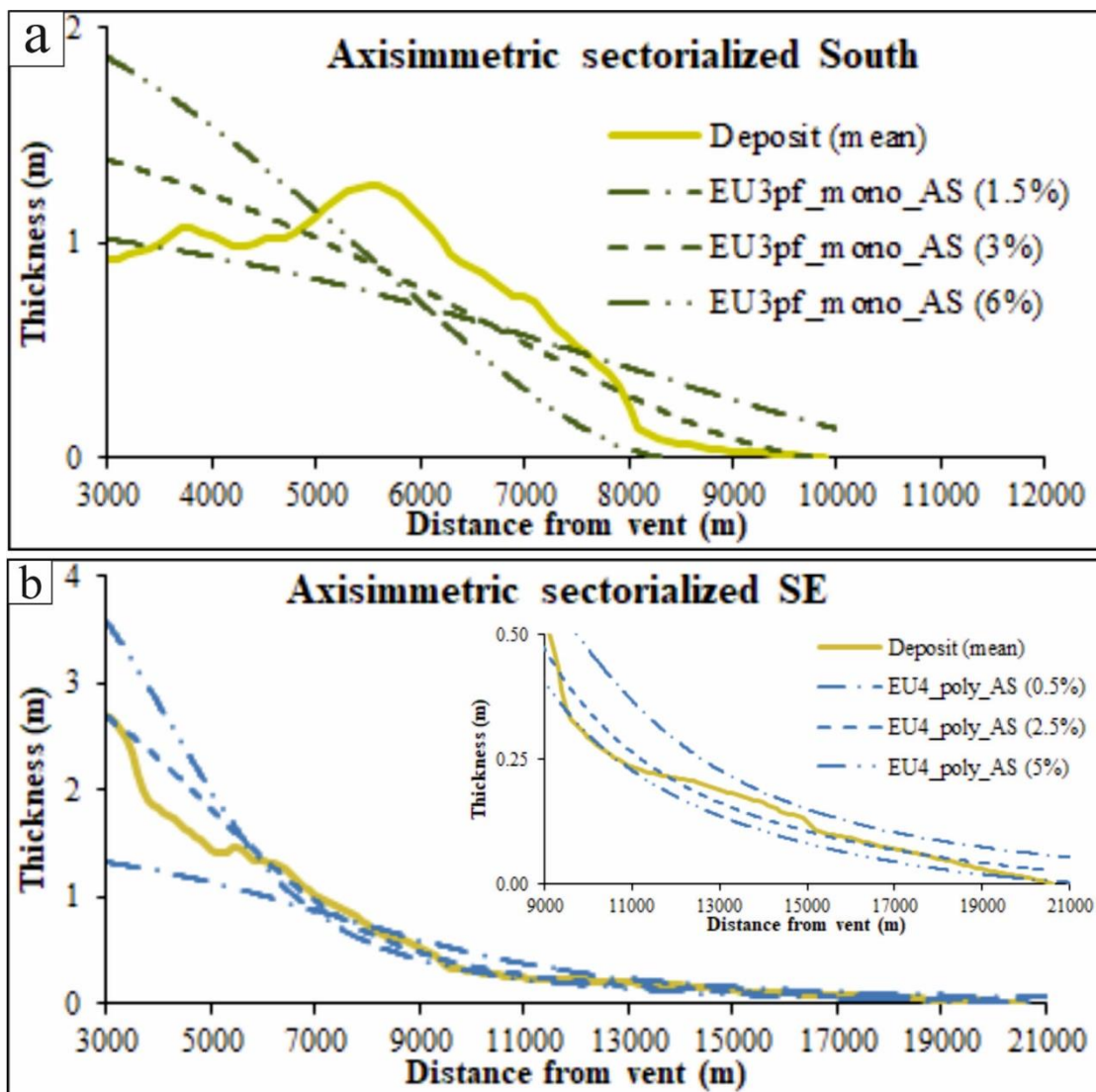330   Different boxes concern different circular sectors.

Figure 7. Comparison between simulations (dashed lines) assuming different initial volumetric fractions of solid particles (ε_0), and the actual deposit (solid line), of the a) EU3pf unit S and b) EU4b/c unit SE. In (b), the inset is a magnification of the thicknesses further than 9 km from the vent.
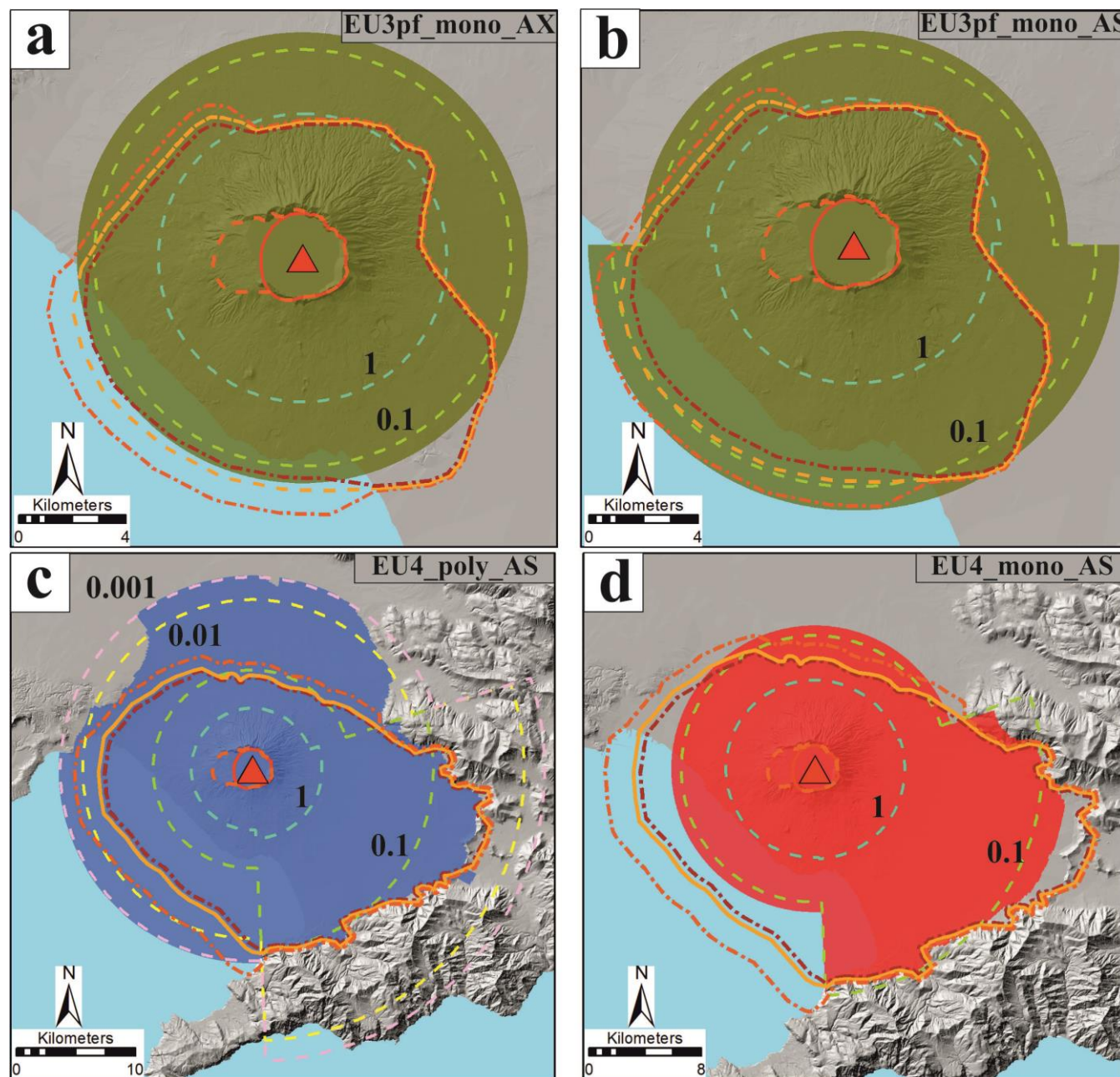
335

Figure 8. Inundation area of the simulations of the EU3pf (a-b) and EU4b/c (c-d) units. The dashed lines represent the theoretical isopachs (in m) of the simulated deposit. Vent location (red triangle), vent uncertainty area (red line) and SV caldera (orange dashed line) as in Tadini et al. (2017). MRLs as in Figure 3. The DEM used in the simulations and as a background derives from Tarquini et al. (2007) according to the modifications explained in section 4.

Simulation	MRL Percentile	TP	FP	TN
EU3pf_mono_AX	5th	66%	32%	2%
	50th	67%	29%	4%
	95th	65%	25%	10%
EU3pf_mono_AS	5th	63%	37%	0%
	50th	67%	32%	0.001%
	95th	75%	24%	0.3%
EU4_poly_AS	5th	61%	38%	0.7%
	50th	64%	35%	1%
	95th	73%	24%	2%
EU4_mono_AS	5th	80%	8%	11%
	50th	78%	7%	15%
	95th	73%	3%	24%

Table 5. True Positive (TP), False Positive (FP) and True Negative (TN) instances of the simulations in Figure 8.
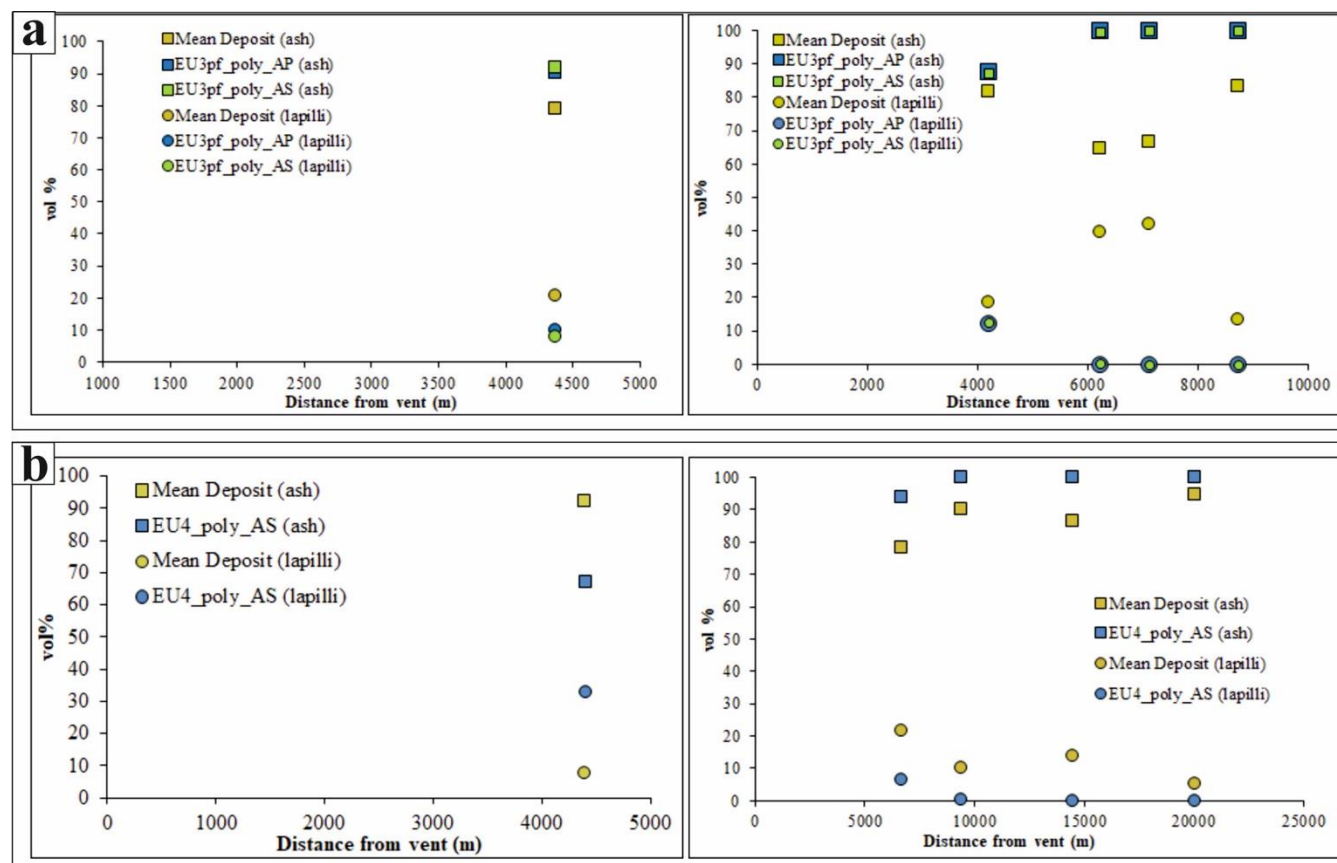
345 **Figure 9**. Volumetric content of ash/lapilli of model/deposit with distance to the source, of the units a) EU3pf N/S (left and right respectively) and b) EU4b/c NW/SE (left and right respectively).
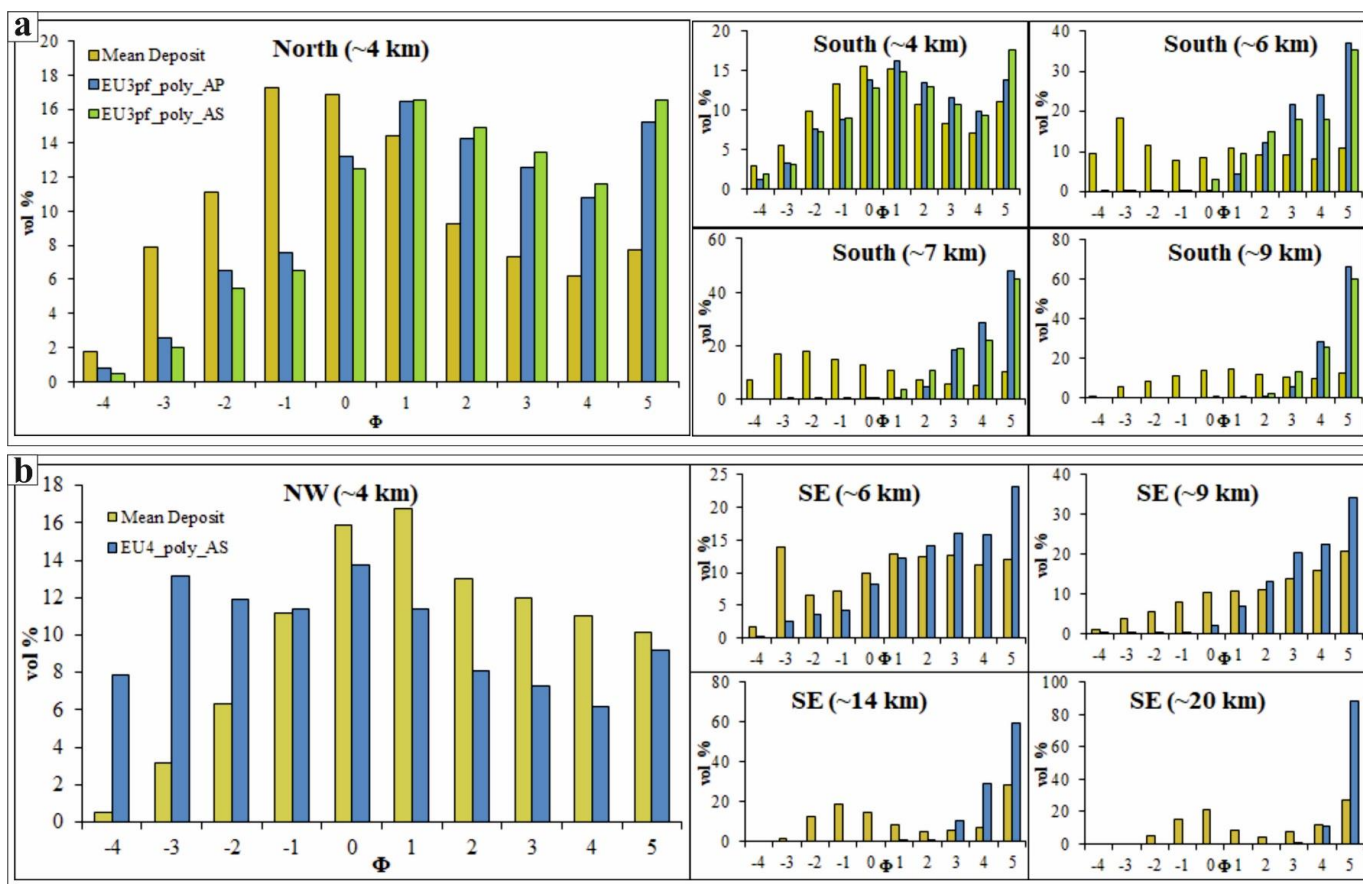
Figure 10. Comparison of volumetric grain sizes of the a) EU3pf and b) EU4b/c units. Different boxes concern different distances to the source.

Solid Earth
Discussions

Open Access

EGU

5 Analysis and discussion

350 **5.1 General considerations**

Testing PyBox with respect to field data is aimed at two main objectives: i) quantifying the degree of reproduction of the real PDC deposit of Plinian eruptions in terms of thickness, inundation area and grain size and ii) evaluating the reliability of the code when considering different assumptions, i.e. polydisperse vs. monodisperse situations, and 360° axisymmetric conditions vs dividing circular sectors. Before commenting our results, two main general considerations, in common for both

355 EU3pf and EU4b/c, deserve a special discussion.

5.1.1 Runout truncation and non-deposited material

~~We remind that~~ PyBox ~~code~~ produces the map of the inundated area (Neri et al., 2015; Bevilacqua, 2016), by truncating the runout wherever the kinetic energy of the flow is lower than the potential energy associated ~~to~~ a topographic obstacle (Section 2.1 and Appendix A). In this way, however, the material that lies beyond the truncation is neither redistributed nor

360 considered any more. However, depending on the topography in our case study, this amount of material is not extremely high. For instance, EU4_poly_AS (Table 4), in its SE part, has several truncations due to the intersection of the decay function of kinetic energy with several topographic barriers, i.e. the Apennines to the ENE and the Sorrentina Peninsula to the SE (Figs. 2 and 7). For the whole SE part of the deposit, the topographic barriers are located between 11.85 km and 19.25 km from vent area, with a mean vale of 15 km. If we truncate PyBox deposit in correspond~~ence of~~ these three limits, the

365 non-deposited volume is between 3.46×10^6 m^3 (cut at 19.25 km) and 2.3×10^7 m^3 (cut at 11.85 km), with a mean value of 1.27×10^7 m^3 (cut at 15 km). Considering that the volume collapsed to the SE is 1.5×10^8 m^3, the non-deposited volume corresponds therefore to a value between 2% and 15%, with a mean of 8%. The amount of volume effectively "lost" is relatively small, also considering that the total volume of the collapsing mixture is inclusive of the EU4c unit (co-ignimbritic part). However, further development of the code might consider a strategy to redistribute this non-deposited material (e.g.,

370 Aravena et al., 2020).

5.1.2 Initial volumetric fraction of solid particles

The value of the initial volumetric fraction of solid particles (ε_0) in the PDC represents one of the most uncertain parameters, for which few constraints exist. Recently, Valentine (2020) performed several multiphase simulations using mono- or bi-disperse distributions to investigate the initiation of PDCs from collapsing mixtures, and to derive criteria to determine when

375 either a depth-averaged model or a box-model are best suited to be employed for hazard modelling purposes. The author concluded that, among other factors (e.g. impact speed or relative proportion of fine to coarse particles), a volumetric concentration of particles of around 1% (slightly lower than those used in this paper) is generally capable of producing a dense underflow and a dilute, faster overriding flow. For such cases, ~~and considering an impacting mixture consisting of at least ca. 50% coarse particles (> 1 cm diameter) relative to fines (< 1 cm diameter),~~ Valentine (2020) suggests that a depth-

380 averaged granular flow model well approximates such ~~PDCs,~~ and could be reasonably used for hazard assessment purposes.

For the units studied here, the sedimentological features show that there are clear evidences of the formation of a dense underflow in, respectively, the N part of Somma-Vesuvius volcano (EU3pf unit; Gurioli et al., 1999) and in correspondence of the urban settlements of Herculaneum and Pompeii (EU4 unit; Cioni et al., 1999; Gurioli et al., 2002). We however think the employment of a box-model is justified for at least the unit EU4b/c, which can be considered intermediate between a dilute, turbulent and a granular concentrated current, in the sense of Branney and Kokelaar (2002), but closer to the dilute end-member type. In this view, the box-model can be effectively employed to describe the overriding dilute part units similar to the EU4, following a two-layer approach (Kelfoun, 2017; Valentine, 2020).

For the box-model used here, it should be kept in mind the variation of the ε_0 value might have an important effect on the simulated deposit thicknesses, as seen in Figure 7. In both units, in fact, the model results for thickness at the beginning of the simulated area (i.e. 3 km from vent area), vary from ca. 1 to ca. 2 m (for EU3pf) or from ca. 1.2 m to ca. 3.6 m (for EU4b/c) if ε_0 is varied, respectively, from 1.5% to 6% and from 0.5% to 5%.

5.2 Thickness comparison

The first parameter that we compare between the deposit and the modelled results is the thickness variation with the distance to the source, an approach already adopted, for instance, by Dade and Huppert (1996).

Our comparison focuses on the average thickness calculated over concentric circles drawn with a 100-m step of distance. However, the thickness variation of the deposit in different radial directions describes two different situations for the EU3pf and EU4b/c units and deserves a brief discussion, detailed in Appendix B.

The average thickness of the EU3pf deposit mean profile initially shows an increasing trend (between 3 to 4 km to the N and between 3 to 6 km to the S – Fig. 6a) followed by a slow, constant decrease. This situation could highlight a lower capability of the current to deposit in more proximal areas, allowing the mass to be redistributed toward more distal sections. This could also be motivated with a spatial variation of the PDC flux regime, which was more turbulent in proximal areas than in distal ones, as also testified by the abundance of lithofacies typical of dilute and turbulent PDCs (//LT to xsLT; see Fig. 2b and Gurioli et al., 1999). Instead, the spatial homogeneity of lithofacies for the EU4b/c unit (Cioni et al., 1992) suggests a higher uniformity of its parent PDC. Moreover, the trend of the mean deposit thickness profile has a steep and rapid decrease of thickness up to 5-6 km, followed (after a break in slope) by a "tail" with an increasing gentler decrease of thickness. This peculiar trend is in agreement with the lithofacies association in the unit EU4b/c (Cioni et al., 1992), which indicate a progressive dilution of the current through time and a progressive aggradation of the deposit.

That said, the degree of matching between the modelled and the real thickness of the EU3pf unit is less accurate than in the EU4b/c case study. However, the mean thickness profile of the actual deposit is roughly parallel with the model, in some parts. Under polydisperse conditions, PyBox does not improve its performance in replicating the thickness profile of EU3pf. The difficulties of PyBox in reproducing the thickness average profile ~~testifies the strongest interaction of the EU3pf unit with the non-homogeneous topography (see also Gurioli, 1999; Cioni et al., 2020) and~~ the likely dominant role of the density stratification and granular transport in the deposition process. To the North there was in fact an extremely rough topography,

21

415 ~~similar to the present one,~~ where the interaction of the PDC with the surface produced largely variable lithofacies. To the South instead there was a gentler topography, with a topographic high on which the town of Pompeii (see Fig. 2a) was built. This latter aspect is also evident from Vogel and Märker (2010), who reconstructed the pre-AD79 paleotopography of the plain to the SE of the SV edifice. From this work, it is possible to appreciate how the modelled depth of the pre-AD79 surface is 0-1 m lower with respect to the present surface in correspondence of the present town of Pompeii and the ancient Pompeii excavations (due to the presence of piles of tephra fallout deposits up to 2 m thick), while it is up to 6-7 m deeper to

420 the NW of these sites.

The thickness comparison of the EU4b/c unit, on the contrary, suggests that this unit was likely deposited under inertial flow conditions, dominated by turbulent transport. The SE "tail" part of the deposit is particularly very well reproduced by the polydisperse simulations, where the simulated profile is almost coincident with the deposit profile (Fig. 6b – right). Conversely, to the NW the modelled thickness in the initial part overestimates a bit the real deposit (Fig. 6b). The

425 polydisperse simulations (blue dashed lines in Fig. 6b) are much closer to the measured trend of the mean thickness profile than under the monodisperse conditions (i.e. MSD), demonstrating the key role of the grain-size distribution in gas-particle turbulent transport.

5.3 Comparison of inundated areas

430 The areal overlapping between the model output area and the actual deposit (True Positive - TP) is discussed together with the quantification of model overestimation (False Positive - FP) and underestimation (True Negative - TN). In Table 5 we also provided the TP/FP/TN estimates also for the 5th and 95th percentiles of the maximum runout lines (MRLs), i.e. a measure of the spatial uncertainty affecting the actual deposit. We remark that the TN instances could be interesting from a hazard point of view, because they actually represent the underestimation of the model: a conservative approach is therefore

435 to use the lowest value of the TN instances as a threshold to evaluate the reliability of a model.

As said above, the polydisperse simulations of the EU3pf unit poorly fit with the deposit thickness, and the inundated area is significantly larger than the deposit area. Thus, they are not included in the quantitative estimation of area match/mismatch. For instance, while the maximum runouts of the deposit are on the order of 8-10 km, the maximum runout given by the model (in absence of topography) is ca. 13-15 km. The monodisperse simulations perform better, in this sense, and

440 maximum runouts are slightly different (ca. 7-10 km) from the real ones: for this reason, only the monodisperse simulations for the EU3pf case have been considered in Figure 8 and Table 5. More precisely, the axisymmetrical (EU3pf_mono_AX) and the sectorialized (EU3pf_mono_AS) share a similar degree of TP instances (between 63% and 75% - Table 5), but have opposite properties for what concerns overestimation/underestimation. EU3pf_mono_AX has in fact a higher tendency to underestimate (FP < TN – Table 5) while EU3pf_mono_AS tends to overestimate the actual deposit (FP > TN – Table 5).

445 For what concerns the EU4b/c simulations (Fig. 8), we report the quantitative matching of both the simulations under polydisperse and monodisperse conditions. The most striking feature that could be seen from Figure 8 is that, while to the SE

a good matching is obtained, to the NW the polydisperse simulation ~~tends to sensibly~~ overestimate the inundation area. Conversely, the monodisperse simulation is more equilibrate between NW and SE. This could be motivated, for the SE part, ~~with~~ the surrounding morphology of the Sorrentina Peninsula and the Apennines, which acts as a natural barrier, and, for the

450 NW sector, to the absence of morphological constraints especially to the N. The results presented in Fig. 8 and Table 5 show that the TP values for the simulation EU4_poly_AS are in the interval 61%-73%, while TN values range from 0.7% and 2%, and FP values range from 24% and 38%. Thus, while the degree of overlapping between model and deposit is at an acceptable value and the percentage of model underestimation is below 2%, the model tends to appreciably overestimate the median outline of the deposit. On the opposite, the simulation EU4_mono_AS shows the highest TP values (73%-80%) and

455 the lowest FP (3%-8%). Despite these better performances, it should be ~~always reminded~~ how the thickness profile is less accurate under monodisperse conditions.

~~We remark that,~~ beyond 14 km (ca. 2-3 km beyond the deposit MRL$_{95}$) the thickness provided by the model under polydisperse conditions is < 1 mm (see Figure 8c). ~~Shallow~~ deposits might be possibly affected by erosion, and the actual deposit in the NW sector might in fact resemble the PyBox results. We also ~~remark~~ that the MRLs defined by Cioni et al.

460 (2020) have been defined up the 95th percentile, meaning that there is still a 5% chance that the actual MRL could be placed further away from the source. This is very significant in the NW part of the EU4b/c deposit, where no or very few outcrops can be found beyond 5-6 km from vent area.

5.4 Grain size comparison

Finally, we consider the volume fraction of the grain sizes of the actual deposits versus those derived from PyBox. We

465 present the results in two different ways. Firstly, we provide a general overview of what are the relative proportions of ash/lapilli with distance to the source (Fig. 9), and then we provide more complete volumetric grain size comparisons for each Φ unit (Fig. 10). ~~We note that this~~ comparison is one of the most uncertain because of some inherent epistemic uncertainties in the data~~, that are~~: i) the complete lack of ultra-proximal sites possibly enriched in coarse grained particles that influenced the calculated TGSD; ii) the fact that the sections used for TGSD calculation and data comparison are (for

470 both units) located mainly along the aprons of the volcano, in many cases in correspondence of the lower parts of valleys or paleovalleys. This could have led to have an under-representation of the finer-grained deposits located in high or paleo-high morphological locations.

The data presented in Fig. 9 confirms the differences between EU3pf and EU4b/c. EU3pf (Fig. 9a) shows that the simulated and real volumetric contents of ash/lapilli are similar only up to 4 km (both to the N and to the S). Then, the relative

475 proportions of ash/lapilli in the simulations indicate that, after 6 km, the simulated grain sizes are made almost entirely (>90%) by ash, with a sensitive difference with respect to field data (only to the S, as to the N there are no available measurements). The most extreme situation could be seen at 9 km, where the modelled grain sizes are composed for > 80% in volume by the two finest ones (4Φ-5Φ), while deposit data indicate a more equal distribution of grain sizes. In Fig. 10a we

observe that at 4 km (both N and S) the grain size distributions are similar between the actual deposit and the model,

480 although there is a shift of ca. 2 Φ toward the finer grain sizes in the modelled data.

For the EU4b/c unit, we observe that the general proportions between ash and lapilli (Fig. 9b) are more similar between the model and the deposit (especially at 4 km from the vent area to the N). However, in Fig. 10b we see that at 4 km to the N, the situation is opposite to EU3pf, since the modelled grain size is richer in coarse particles than the actual deposit. Such difference might be motivated with the above-mentioned roughness of the topography, which might favour the deposition of

485 coarser particles at locations < 4 km. In the SE sector the differences between modelled and observed grain sizes are lower at 6 km and 9 km distance to the source, while are greater at 14 km and 20 km, where the 2 finest modelled grain sizes account for > 80% of the volume.

6 Conclusions

We have evaluated the suitability of the box-model approach implemented in the PyBox code to reproduce the deposits of

490 EU3pf and EU4b/c, two well-studied PDC units from different phases of the AD 79 Pompeii eruption of Somma-Vesuvius (Italy). The total volume, the TGSD, the grain densities, and the temperature obtained from the field data are used as the main inputs of PyBox. The model produces several outputs that can be directly compared with the inundation areas and radially-averaged PDC deposit features, namely the unit thickness profile and the grain size distribution as a function of the radial distance to the source. We have performed simulations either under polydisperse or monodisperse conditions, given

495 by, respectively, the total grain size distribution and the mean Sauter diameter of the deposit. We have tested axisymmetrical collapses either round-angle or divided in two circular sectors.

The initial volumetric fraction ε_0 of the solid particles over the gas is the main tuning parameter (given its uncertainty) that is explored to fit the outputs with the field data. In this study, we obtained the best fit of deposit data with a plausible initial volume concentration of solid particles from 3% to 6% for EU3pf (depending on the circular sector) and of 2.5% for EU4b/c.

500 These concentrations optimize the reproduction of the thickness profile of the actual deposits.

Concerning the EU3pf unit: 1) the average thickness of the EU3pf deposit initially shows an increasing trend, from 3 to 4 km to the N and from 3 to 6 km to the S, followed by a slow, constant decrease. The simulated thickness poorly resembles the actual deposit, although the maximum values are comparable and the two profiles are roughly parallel, in some parts. Under

505 polydisperse conditions, PyBox does not improve its performance in reproducing the thickness profile of EU3pf; 2) in the monodisperse simulations of EU3pf the maximum runouts are slightly different from the real ones, but overall consistent. The round-angle and sectorialized simulations share a similar degree of TP instances (between 63% and 75%), but have opposite properties for what concerns overestimation/underestimation. The round-angle axisymmetric simulation underestimates the actual deposit (FP < TN) while the sectorialized simulation overestimates the actual deposit (FP > TN); 3)

510 the simulated and real volumetric contents of ash/lapilli in EU3pf are similar only up to 4 km. Then, the relative proportions

of ash/lapilli in the simulations indicate that the simulated grain sizes are made almost entirely (>90%) by ash, with a sensitive difference with respect to field data after 6 km. We observe that at 4 km the grain size distributions are similar between the actual deposit and the model, although there is a shift of ca. 2 Φ toward the finer grain sizes in the modelled data.

515 Concerning instead the EU4b/c unit: 1) this unit has a steep and rapid decrease of thickness up to 5-6 km, followed, after a break in slope, by a "tail" with a gentler decrease of thickness. The polydisperse box-model simulations are much closer to the measured trend of the mean thickness profile than under the monodisperse conditions. The SE thickness profile of the polydisperse simulation is almost coincident (within the uncertainty range) with the corresponding part of the deposit (specifically after 6 km, and with a ca. 0.5 m overestimation between 3.5-6 km), while to the NW the modelled thickness

520 slightly overestimates the real deposit in the initial part (up to ca. 6 km); 2) in the simulations of EU4b/c, a good matching of inundated area towards the South-East is obtained. Towards the North-West the polydisperse simulation sensibly overestimates the inundation area. On the opposite, the simulation under monodisperse conditions shows the highest TP values (73%-80%) and the lowest FP (3%-8%). However, the thickness profile is less accurate under monodisperse conditions. Moreover, shallow deposits in the NW sector might be possibly affected by erosion, and the actual deposit in the

525 NW sector might in fact resemble the PyBox results obtained under polydisperse conditions; 3) the general proportions between ash and lapilli in EU4b/c are similar between the model and the deposit. However, at 4 km to the N, the situation is opposite to EU3pf, since the modelled grain size is richer in coarse particles than the actual deposit. In the SE sector the differences between modelled and observed grain sizes are lower at 6 km and 9 km distance to the source, while are greater at 14 km and 20 km, where the 2 finest modelled grain sizes account for > 80% of the volume; 4) in the SE sector, because

530 of model runout truncation, we evaluated an average non-deposited volume of 1.27×10^7 m^3 (cut at 15 km). Considering that the volume collapsed to the SE is 1.5×10^8 m^3, the average non-deposited volume corresponds therefore to a value of 8%. Thus, the amount of volume effectively "lost" with the PyBox approach is relatively small, also considering that the total volume of the collapsing mixture is inclusive of the co-ignimbritic part.

535 Pyroclastic density currents generated by Plinian eruptions span over a wide range of characters, and can display very different behaviour and interaction with the topography. During the AD 79 eruption of Somma-Vesuvius, two PDC units, despite both emplaced after column collapses, display significantly different sedimentological features and should likely be better described by different models. The study findings indicates that the box-model, which is suited to describe turbulent particle-laden inertial gravity currents, well describes the EU4b/c PDC unit but is not able to accurately catch some of the

540 main features of the EU3pf unit. This is probably due to its strongly stratified features, which make the interaction with the topography of the basal concentrated part of the flow a controlling factor in the deposition process. In particular, results highlight again the key role of the grain-size distribution in the description of inertial PDCs: while the final runout is mostly controlled by the finest portion of the distribution, the total grain size distribution strongly affects the thickness profile (e.g., Fig. 6b) and it is an essential ingredient for proper modelling of the PDC dynamics.

545 Our study also highlights the importance of assuming axisymmetric or sectorial propagation of the PDCs. This is an additional source of uncertainty in Plinian (VEI 5) eruptions, in which PDC are often generated by asymmetric column collapse. In the reproduction of a specific deposit unit, considerations about different propagation along specific sectors should be done.

In conclusions, while the box-model approach is certainly suited to describe large volume (VEI > 6) low aspect ratio
550 ignimbrites, some care should be put when applied to smaller PDC-forming eruptions on stratovolcanoes, since the topographic effects due to flow stratification, not considered by the model, might be dominantly important. ~~W~~e believe that ~~such~~ approach, despite its simplifying assumptions, well represents the behaviour of PDCs emplaced under turbulent conditions, in ~~which~~ the effects of the topography on the transport system are negligible, and can be used to assess the hazards associated to this type of flows.

555 **Appendix A: Numerical solution of the box model equations in the PyBox code**

The set of equations of PyBox is numerically integrated by using a 2D embedded Runge-Kutta 3(2) method, following the scheme proposed in Bogacki and Shampine (1989). With respect to the more widely used Runge-Kutta 4(5), this approach is preferred because it succeeds in preserving the monotonicity of the settling solid fractions. In particular, we solve the box model equations with the function scipy.integrate.solve_IVP, available in Python- 3.x. We specifically considered the case
560 when the computed solid fractions numerically fall below zero. We avoided this situation by interrupting the integration process whenever at one or more solid fractions become lower than zero, or extremely small. We restart the process with a new initial value obtained by setting to zero such fractions. The solver is also interrupted when the reduced gravity g' falls below zero, regardless of the values of the solid fractions. The asymptotic, stationary settling velocities of the particle classes are calculated by means of the Newton's impact formula (Dellino et al., 2005; Dioguardi et al., 2018), where the gas-particle
565 drag coefficient C_D^i is defined as a function of the relative gas-particle Reynolds number Re. The computation of settling velocities required an iterative procedure: in fact, the Newton's impact formula was solved together with the relationship for the Reynolds number and the correlation between C_D^i and Re. In particular, we used the Schiller-Naumann correlation (Crowe et al., 2011), which accurately describes the drag force acting on a sphere with Re < 1000, whereas, for Re > 1000, we have set $C_D^i = 1$, according to Woods and Bursik (1991).

570

Appendix B: Deposit thickness variations depending on the radial direction

Figure A1 describes the range of variability of the units' thickness collected in different locations. In EU3pf, a large variability, from 0 to 7.5 m in the N sector, and from 0 to 5 m in the S sector, can be observed. This reflects how the EU3pf unit complexly interacted with the rugged topography that characterizes the aprons of the SV volcano. On the other side, for

575 the EU4b/c unit the differences between deposit thicknesses from maximum and minimum are typically lower, i.e. from 0 to

4 m in the NW sector, and from 0 to 5.5 m in the SE sector.
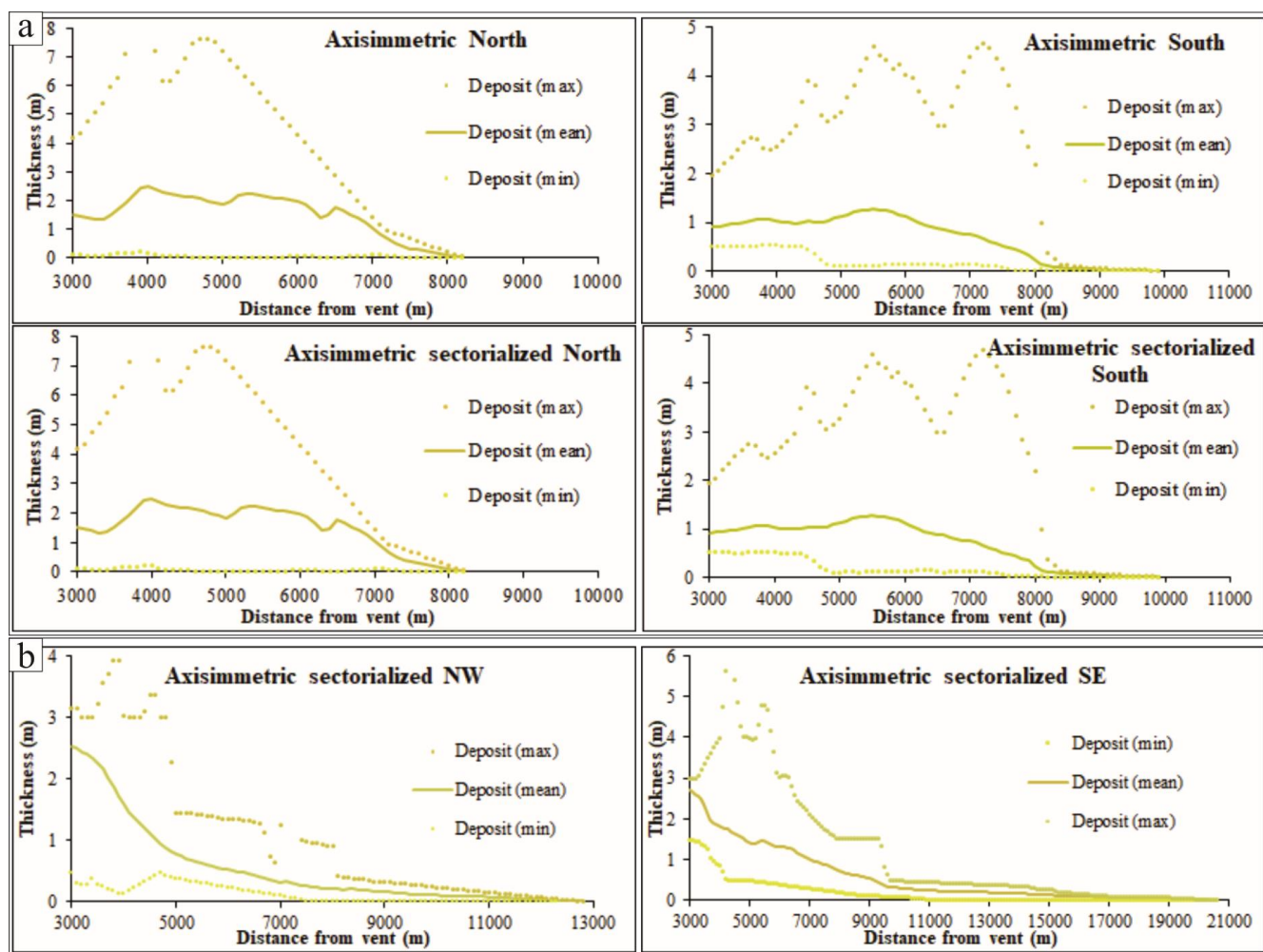
Figure A1. Deposit thickness for a) EU3pf and b) EU4b/c units. "Max", "Mean" and "Min" refer to, respectively, the

580 maximum, mean and minimum thicknesses measured along each circle described in section

Solid Earth
Discussions

Code availability

PyBox is available at http://www.pi.ingv.it/progetti/eurovolc/#VA.

Data availability

Modelled data are available in the supporting information and upon request. Field data used as input parameters are available
585   from the supporting information (https://doi.org/10.6084/m9.figshare.12506027) of Cioni et al. (2020).

Author's contributions

All authors: Conceptualization, Methodology, Writing – Review and Editing; **A. Tadini**: Validation, Formal Analysis,
Investigation, Resources, Data Curation, Writing - Original Draft, Visualization; **A. Bevilacqua**: Software, Validation,
Formal Analysis, Data Curation, Writing - Original Draft; **A. Neri**: Project administration, Funding acquisition; **R. Cioni**:
590   Project administration, Funding acquisition, Resources; **G. Biagioli, M. de' Michieli Vitturi and T. Esposti Ongaro**:
Software, Data Curation.

Competing interests

The authors declare that they have no conflict of interest.

Acknowledgements

References

Aravena, A., Cioni, R., Bevilacqua, A., de' Michieli Vitturi, M., Esposti Ongaro, T., and Neri, A.: Tree-branching based
605   enhancement of kinetic energy models for reproducing channelization processes of pyroclastic density currents, Journal of
Geophysical Research: Solid Earth, https://doi.org/10.1029/2019JB019271, 2020.

Aspinall, W. P., Bevilacqua, A., Costa, A., Inakura, H., Mahony, S., Neri, A., and Sparks, R. S. J.: Probabilistic
reconstruction (or forecasting) of distal runouts of large magnitude ignimbrite PDC flows sensitive to topography using
mass-dependent inversion models, AGU Fall Meeting 2019, San Francisco, CA, USA, 2019,

610   Barberi, F., Cioni, R., Rosi, M., Santacroce, R., Sbrana, A., and Vecci, R.: Magmatic and phreatomagmatic phases in
explosive eruptions of Vesuvius as deduced by grain-size and component analysis of the pyroclastic deposits, Journal of
volcanology and geothermal research, 38, 287-307, 1989.

Benjamin, T. B.: Gravity currents and related phenomena, Journal of Fluid Mechanics, 31, 209-248,
https://doi.org/10.1017/S0022112068000133, 1968.

615   Bevilacqua, A.: Doubly stochastic models for volcanic vent opening probability and pyroclastic density current hazard at
Campi Flegrei caldera, Classe di Scienze - Matematica per le tecnologie industriali, Scuola Normale Superiore, Pisa, 184
pp., 2016.

Bevilacqua, A., Neri, A., Bisson, M., Esposti Ongaro, T., Flandoli, F., Isaia, R., Rosi, M., and Vitale, S.: The effects of vent
location, event scale, and time forecasts on pyroclastic density current hazard maps at Campi Flegrei caldera (Italy),
620   Frontiers in Earth Science, 5, 72, https://doi.org/10.3389/feart.2017.00072, 2017.

Bevilacqua, A.: Notes on the analytic solution of box model equations for gravity-driven particle currents with constant
volume, 2019.

Bevilacqua, A., de'Michieli Vitturi, M., Esposti Ongaro, T., and Neri, A.: Enhancing the uncertainty quantification of
pyroclastic density current dynamics in the Campi Flegrei caldera. , Frontiers of Uncertainty Quantification, Pisa (Italy),
625   2019a,

Bevilacqua, A., Patra, A. K., Bursik, M. I., Pitman, E. B., Macías, J. L., Saucedo, R., and Hyman, D.: Probabilistic
forecasting of plausible debris flows from Nevado de Colima (Mexico) using data from the Atenquique debris flow, 1955,
Natural Hazard and Earth System Sciences, 19, https://doi.org/10.5194/nhess-19-791-2019, 2019b.

Biagioli, G., Bevilacqua, A., Esposti Ongaro, T., and de' Michieli Vitturi, M.: PyBox: a Python tool for simulating the
630   kinematics of Pyroclastic density currents with the box-model approach Reference and User's Guide, 2019.

Bogacki, P., and Shampine, L. F.: A 3 (2) pair of Runge-Kutta formulas, Applied Mathematics Letters, 2, 321-325,
https://doi.org/10.1016/0893-9659(89)90079-7, 1989.

Bonnecaze, R. T., Hallworth, M. A., Huppert, H. E., and Lister, J. R.: Axisymmetric particle-driven gravity currents, Journal
of Fluid Mechanics, 294, 93-121, https://doi.org/10.1017/S0022112095002825, 1995.

635 Branney, M. J., and Kokelaar, B. P.: Pyroclastic density currents and the sedimentation of ignimbrites, Memoirs, Geological Society, London, 143 pp., 2002.

Breard, E. C. P., Dufek, J., and Lube, G.: Enhanced mobility in concentrated pyroclastic density currents: An examination of a self-fluidization mechanism, Geophysical Research Letters, 45, 654-664, https://doi.org/10.1002/2017GL075759, 2018.

Bursik, M. I., and Woods, A. W.: The dynamics and thermodynamics of large ash flows, Bulletin of Volcanology, 58, 175-
640 193, https://doi.org/10.1007/s004450050134, 1996.

Cepeda, J., Chávez, J. A., and Martínez, C. C.: Procedure for the selection of runout model parameters from landslide back-analyses: application to the Metropolitan Area of San Salvador, El Salvador, Landslides, 7, 105-116, 2010.

Charbonnier, S. J., and Gertisser, R.: Numerical simulations of block-and-ash flows using the Titan2D flow model: examples from the 2006 eruption of Merapi Volcano, Java, Indonesia, Bulletin of Volcanology, 71, 953-959, 2009.

645 Charbonnier, S. J., Palma, J. L., and Ogburn, S.: Application of" shallow-water" numerical models for hazard assessment of volcanic flows: the case of TITAN2D and Turrialba volcano (Costa Rica), Revista Geológica de América Central, 107-128, 2015.

Cioni, R., Marianelli, P., and Sbrana, A.: Dynamics of the AD 79 eruption: Stratigraphic, sedimentological and geochemical data on the successions from the Somma-Vesuvius southern and eastern sectors, Acta Vulcanologica, 2, 109-123, 1992.

650 Cioni, R., Santacroce, R., and Sbrana, A.: Pyroclastic deposits as a guide for reconstructing the multi-stage evolution of the Somma-Vesuvius Caldera, Bulletin of Volcanology, 61, 207-222, 1999.

Cioni, R., Gurioli, L., Lanza, R., and Zanella, E.: Temperatures of the AD 79 pyroclastic density current deposits (Vesuvius, Italy), Journal of Geophysical Research: Solid Earth, 109, https://doi.org/10.1029/2002JB002251, 2004.

Cioni, R., Tadini, A., Gurioli, L., Bertagnini, A., Mulas, M., Bevilacqua, A., and Neri, A.: Estimating eruptive parameters
655 and related uncertainties for Pyroclastic Density Currents deposits: worked examples from Somma-Vesuvius (Italy), Bulletin of Volcanology, 82, https://doi.org/10.1007/s00445-020-01402-7, 2020.

Crowe, C. T., Schwarzkopf, J. D., Sommerfeld, M., and Tsuji, Y.: Multiphase flows with droplets and particles, CRC press, 2011.

Dade, W. B., and Huppert, H. E.: A box model for non-entraining, suspension-driven gravity surges on horizontal surfaces,
660 Sedimentology, 42, 453-470, 1995a.

Dade, W. B., and Huppert, H. E.: Runout and fine-sediment deposits of axisymmetric turbidity currents, Journal of Geophysical Research: Oceans, 100, 18597-18609, https://doi.org/10.1029/95JC01917, 1995b.

Dade, W. B., and Huppert, H. E.: Emplacement of the Taupo ignimbrite by a dilute turbulent flow, Nature, 381, 509-512, 1996.

665   Dade, W. B., and Huppert, H. E.: Long-runout rockfalls, Geology, 26, 803-806, https://doi.org/10.1130/0091-7613(1998)026<0803:LRR>2.3.CO;2, 1998.

de'Michieli Vitturi, M., Esposti Ongaro, T., Lari, G., and Aravena, A.: IMEX_SfloW2D 1.0: a depth-averaged numerical flow model for pyroclastic avalanches, Geoscientific Model Development, 10.5194/gmd-12-581-2019, 2019.

Dellino, P., Mele, D., Bonasia, R., Braia, G., La Volpe, L., and Sulpizio, R.: The analysis of the influence of pumice shape
670   on its terminal velocity, Geophysical Research Letters, 32, https://doi.org/10.1029/2005GL023954, 2005.

Dioguardi, F., Mele, D., and Dellino, P.: A new one-equation model of fluid drag for irregularly shaped particles valid over a wide range of Reynolds number, Journal of Geophysical Research: Solid Earth, 123, 144-156, https://doi.org/10.1002/2017JB014926, 2018.

Doyle, E. E., Hogg, A. J., Mader, H. M., and Sparks, R. S. J.: A two-layer model for the evolution and propagation of dense
675   and dilute regions of pyroclastic currents, Journal of Volcanology and Geothermal Research, 190, 365-378, 2010.

Esposti Ongaro, T., Cavazzoni, C., Erbacci, G., Neri, A., and Salvetti, M. V.: A parallel multiphase flow code for the 3D simulation of explosive volcanic eruptions, Parallel Computing, 33, 541-560, 2007.

Esposti Ongaro, T., Orsucci, S., and Cornolti, F.: A fast, calibrated model for pyroclastic density currents kinematics and hazard, Journal of Volcanology and Geothermal Research, https://doi.org/10.1016/j.jvolgeores.2016.08.002, 2016.

680   Esposti Ongaro, T., Komorowski, J. C., De'Michieli Vitturi, M., and Neri, A.: Computer Simulation of Explosive Eruption Scenarios at La Soufrière de Guadeloupe (FR): Implications for Volcanic Hazard Assessment, AGUFM, 2019.

Fan, L. S., and Zhu, C.: Size and Properties of Particles, in: Principles of gas-solid flows, edited by: Fan, L. S., and Zhu, C., Cambridge University Press, Cambridge, 1998.

Fauria, K. E., Manga, M., and Chamberlain, M.: Effect of particle entrainment on the runout of pyroclastic density currents,
685   Journal of Geophysical Research: Solid Earth, 121, 6445-6461, https://doi.org/10.1002/2016JB013263, 2016.

Fawcett, T.: An introduction to ROC analysis, Pattern recognition letters, 27, 861-874, 2006.

Gurioli, L.: Flussi piroclastici: classificazione e meccanismi di messa in posto, Department of Earth Sciences, University of Pisa, Pisa, 1999.

Gurioli, L., Cioni, R., and Bertagna, C.: I depositi di flusso piroclastico dell'eruzione del 79 dC caratterizzazione
690   stratigrafica, sedimentologica e modelli di trasporto e deposizione, Atti Soc Tosc Sci Nat Mem Serie A, 106, 61-72, 1999.

Gurioli, L., Cioni, R., Sbrana, A., and Zanella, E.: Transport and deposition of pyroclastic density currents over an inhabited area: the deposits of the AD 79 eruption of Vesuvius at Herculaneum, Italy, Sedimentology, 49, 929-953, 2002.

Gurioli, L., Sulpizio, R., Cioni, R., Sbrana, A., Santacroce, R., Luperini, W., and Andronico, D.: Pyroclastic flow hazard assessment at Somma–Vesuvius based on the geological record, Bulletin of Volcanology, 72, 1021-1038, https://doi.org/10.1007/s00445-010-0379-2, 2010.

Hallworth, M. A., Hogg, A. J., and Huppert, H. E.: Effects of external flow on compositional and particle gravity currents, Journal of Fluid Mechanics, 359, 109-142, https://doi.org/10.1017/S0022112097008409, 1998.

Huppert, H. E., and Simpson, J. E.: The slumping of gravity currents, Journal of Fluid Mechanics, 99, 785-799, https://doi.org/10.1017/S0022112080000894, 1980.

Kelfoun, K., Samaniego, P., Palacios, P., and Barba, D.: Testing the suitability of frictional behaviour for pyroclastic flow simulation by comparison with a well-constrained eruption at Tungurahua volcano (Ecuador), Bulletin of volcanology, 71, 1057, https://doi.org/10.1007/s00445-009-0286-6, 2009.

Kelfoun, K.: Suitability of simple rheological laws for the numerical simulation of dense pyroclastic flows and long-runout volcanic avalanches, Journal of Geophysical Research: Solid Earth, 116, 2011.

Kelfoun, K.: A two-layer depth-averaged model for both the dilute and the concentrated parts of pyroclastic currents, Journal of Geophysical Research: Solid Earth, 122, 4293-4311, https://doi.org/10.1002/2017JB014013, 2017.

Lee, D. T., and Schachter, B. J.: Two algorithms for constructing a Delaunay triangulation, Internat. J. Comput. Inform. Sci., 3, 219-241, 1980.

Malin, M. C., and Sheridan, M. F.: Computer-assisted mapping of pyroclastic surges, Science, 217, 637-640, 10.1126/science.217.4560.637, 1982.

Neri, A., Esposti Ongaro, T., Macedonio, G., and Gidaspow, D.: Multiparticle simulation of collapsing volcanic columns and pyroclastic flow, Journal of Geophysical Research: Solid Earth, 108, https://doi.org/10.1029/2001JB000508, 2003.

Neri, A., Bevilacqua, A., Esposti Ongaro, T., Isaia, R., Aspinall, W. P., Bisson, M., Flandoli, F., Baxter, P. J., Bertagnini, A., and Iannuzzi, E.: Quantifying volcanic hazard at Campi Flegrei caldera (Italy) with uncertainty assessment: II. Pyroclastic density current invasion maps, Journal of Geophysical Research: Solid Earth, https://doi.org/10.1002/2014JB011776, 2015.

Newhall, C. G., and Self, S.: The volcanic explosivity index/VEI/- An estimate of explosive magnitude for historical volcanism, Journal of Geophysical Research, 87, 1231-1238, 1982.

Ogburn, S. E., and Calder, E. S.: The relative effectiveness of empirical and physical models for simulating the dense undercurrent of pyroclastic flows under different emplacement conditions, Frontiers in Earth Science, 5, 83, https://doi.org/10.3389/feart.2017.00083, 2017.

Patra, A. K., Bauer, A. C., Nichita, C. C., Pitman, E. B., Sheridan, M. F., Bursik, M. I., Rupp, B., Webber, A., Stinton, A. J., and Namikawa, L. M.: Parallel adaptive numerical simulation of dry avalanches over natural terrain, Journal of Volcanology and Geothermal Research, 139, 1-21, https://doi.org/10.1016/j.jvolgeores.2004.06.014, 2005.

Patra, A. K., Bevilacqua, A., and Safei, A. A.: Analyzing Complex Models using Data and Statistics, International
725 Conference on Computational Science, 2018, 724-736,

Patra, A. K., Bevilacqua, A., Akhavan-Safaei, A., Pitman, E. B., Bursik, M. I., and Hyman, D.: Comparative analysis of the
structures and outcomes of geophysical flow models and modeling assumptions using uncertainty quantification, Frontiers in
Earth Science, 10.3389/feart.2020.00275, 2020.

Roche, O., Phillips, J. C., and Kelfoun, K.: Pyroclastic density currents, in: Modeling Volcanic Processes: The Physics and
730 Mathematics of Volcanism, edited by: Fagents, S. A., Gregg, T. K. P., and Lopes, R. M. C., Cambridge University Press,
2013.

Sandri, L., Tierz, P., Costa, A., and Marzocchi, W.: Probabilistic hazard from pyroclastic density currents in the Neapolitan
area (Southern Italy), Journal of Geophysical Research: Solid Earth, 123, 3474-3500, https://doi.org/10.1002/2017JB014890,
2018.

735 Santacroce, R., Cristofolini, R., La Volpe, L., Orsi, G., and Rosi, M.: Italian active volcanoes, Episodes Journal of
International Geoscience, 26, 227-234, https://doi.org/10.18814/epiiugs/2003/v26i3/013, 2003.

Sheridan, M. F., and Malin, M. C.: Application of computer-assisted mapping to volcanic hazard evaluation of surge
eruptions: Vulcano, Lipari, and Vesuvius, Journal of Volcanology and Geothermal Research, 17, 187-202, 1983.

Tadini, A., Bisson, M., Neri, A., Cioni, R., Bevilacqua, A., and Aspinall, W. P.: Assessing future vent opening locations at
740 the Somma-Vesuvio volcanic complex: 1. A new information geo-database with uncertainty characterizations, Journal of
Geophysical Research: Solid Earth, 122, 4336-4356, 10.1002/2016JB013858, 2017.

Tarquini, S., Isola, I., Favalli, M., Mazzarini, F., Bisson, M., Pareschi, M. T., and Boschi, E.: TINITALY/01: a new
triangular irregular network of Italy, Annals of Geophysics, 50, 2007.

Tierz, P., Sandri, L., Costa, A., Sulpizio, R., Zaccarelli, L., Di Vito, M. A., and Marzocchi, W.: Uncertainty assessment of
745 pyroclastic density currents at Mount Vesuvius (Italy) simulated through the energy cone model, in: Natural hazard
uncertainty assessment: Modeling and decision support, edited by: Riley, K., Webley, P., and Thompson, M., Geophysical
Monograph Series, Wiley, 125-145, 2016a.

Tierz, P., Sandri, L., Costa, A., Zaccarelli, L., Di Vito, M. A., Sulpizio, R., and Marzocchi, W.: Suitability of energy cone for
probabilistic volcanic hazard assessment: validation tests at Somma-Vesuvius and Campi Flegrei (Italy), Bulletin of
750 Volcanology, 78, 79, https://doi.org/10.1007/s00445-016-1073-9, 2016b.

Tierz, P., Stefanescu, E. R., Sandri, L., Sulpizio, R., Valentine, G. A., Marzocchi, W., and Patra, A. K.: Towards
Quantitative Volcanic Risk of Pyroclastic Density Currents: Probabilistic Hazard Curves and Maps Around Somma-
Vesuvius (Italy), Journal of Geophysical Research: Solid Earth, 123, 6299-6317, 2018.

Valentine, G. A.: Initiation of dilute and concentrated pyroclastic currents from collapsing mixtures and origin of their
755 proximal deposits, Bulletin of Volcanology, 82, 20, https://doi.org/10.1007/s00445-020-1366-x, 2020.

Vogel, S., and Märker, M.: Reconstructing the Roman topography and environmental features of the Sarno River Plain (Italy) before the AD 79 eruption of Somma–Vesuvius, Geomorphology, 115, 67-77, 2010.

Woods, A. W., and Bursik, M. I.: Particle fallout, thermal disequilibrium and volcanic plumes, Bulletin of Volcanology, 53, 559-570, https://doi.org/10.1007/BF00298156, 1991.

760